Supporting Information

Unveiling the Importance of Non-Dominant Facets in (111)-Dominated Perovskite Films

Bo Zhou [a, b], Pei Zhao [d], Junxue Guo [a, e], Shuaifeng Hu [f], Xin Guo [a, b], Jiewei Liu [a, *], Can Li [b, c, *]

[a] *State Key Laboratory of Photoelectric Conversion and Utilization of Solar Energy, Dalian National Laboratory for Clean Energy, Dalian Institute of Chemical Physics, Chinese Academy of Sciences, Dalian 116023, China*
[b] *University of Chinese Academy of Sciences, Beijing 100049, China*
[c] *State Key Laboratory of Catalysis, Dalian Institute of Chemical Physics, Chinese Academy of Sciences, Dalian 116023, China*
[d] *Research Center for Computational Science, Institute for Molecular Science, Okazaki 444-8585, Japan*
[e] *School of Chemistry and Materials Science, University of Science and Technology of China, Hefei 230026, China*
[f] *Clarendon Laboratory, Department of Physics, University of Oxford, Parks Road, Oxford OX1 3PU, U.K.*
* *Corresponding author.*
E-mail: jwliu@dicp.ac.cn ; canli@dicp.ac.cn

This PDF file includes:
Figures S1 to S54
Tables S1 to S5

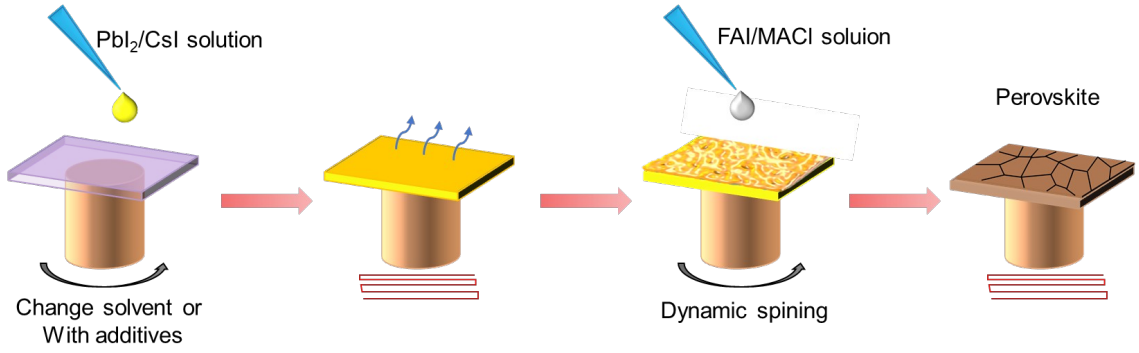

Figure S1. Scheme of the two-step fabrication process of the perovskite films.

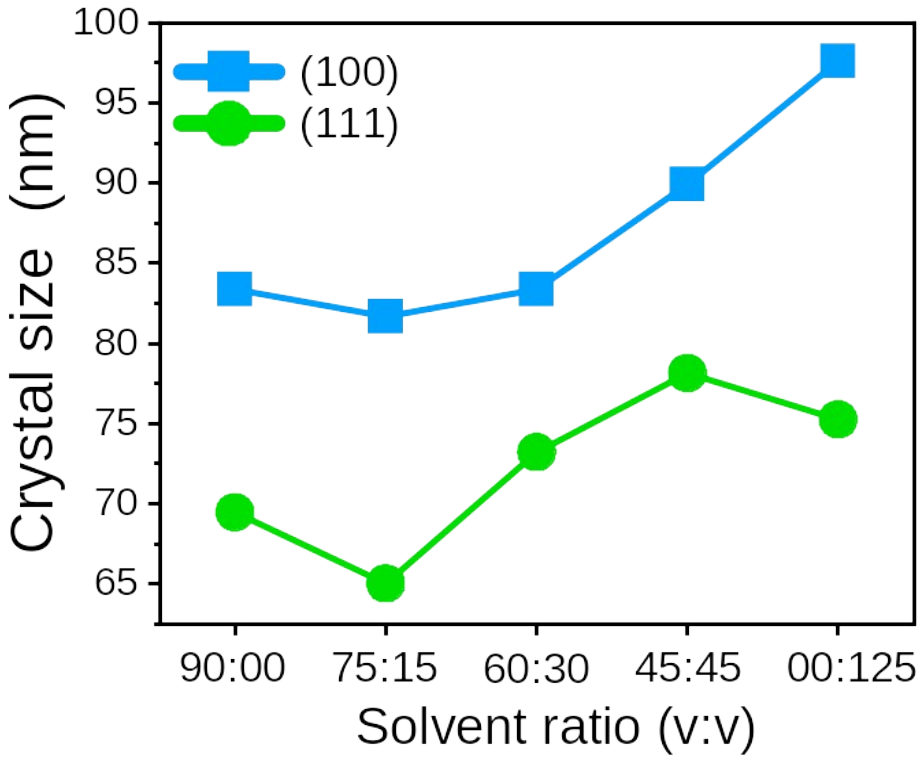

Figure S2. The crystal sizes calculated by the Scherrer formula for (100) and (111) facet under different solvent conditions.

Both the (100) and (111) facets were analyzed separately, revealing that after introducing NMP in the ternary solvent regulation, the crystal size increased under the target conditions following the initial shuffling stage, aligning with the discussion in the manuscript. Further analysis indicates that the (100) facet remains consistently larger than the (111) facet. Aside from

the influence of the shape factor, (100) facets co-exist with (111) facets, which justifies the consideration of non-dominant (100) facets in this work.

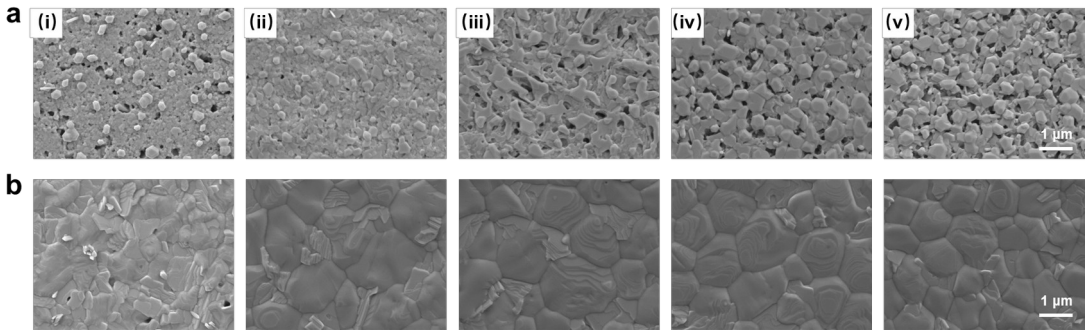

Figure S3. SEM images of the films with different treatments. (a) PbI_2 films after 70 ℃ annealing and (b) the perovskite films after 150 ℃ annealing. (i) DMF:DMSO:NMP = 910:90:0, (ii) DMF:DMSO:NMP = 910:75:15, (iii) DMF:DMSO:NMP = 910:60:30, (iv) DMF:DMSO:NMP = 910:45:45, (v) DMF:DMSO:NMP = 875:0:125.

From the SEM images, it is evident that under the assistance of NMP, the porous and non-dense PbI_2 film becomes flat and dense. This morphology change typically corresponds to the full crystallization of lead iodide.[1] On the other hand, PbI_2 films treated with pure NMP exhibit a more pronounced porous structure with small variations, where PbI_2 sticks intertwine to form a grid-like pattern.

The crystal sizes obtained from XRD calculations can also be correlated with the grain sizes observed in SEM images of Figure S1 in Supporting Information. Generally, individual crystal or crystallite are not directly visible, as the Scherrer formula calculates crystal size rather than grain size. Grains usually consist of one or more aggregated crystallites. Consequently, the grain size observed in SEM is typically larger than the crystal size calculated from XRD. However, the overall trend remains consistent, with larger crystallites under the target conditions. Additionally, the binary DMF/NMP solvent system favors the (100) facet, leading to a smoother facet morphology.

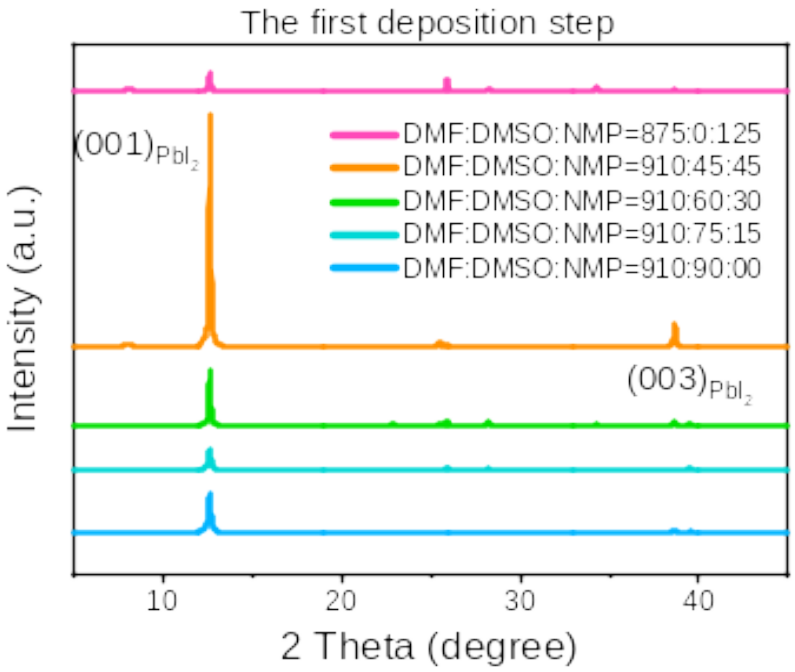

Figure S4. XRD patterns for PbI_2 films with varied ternary solvent ratios.

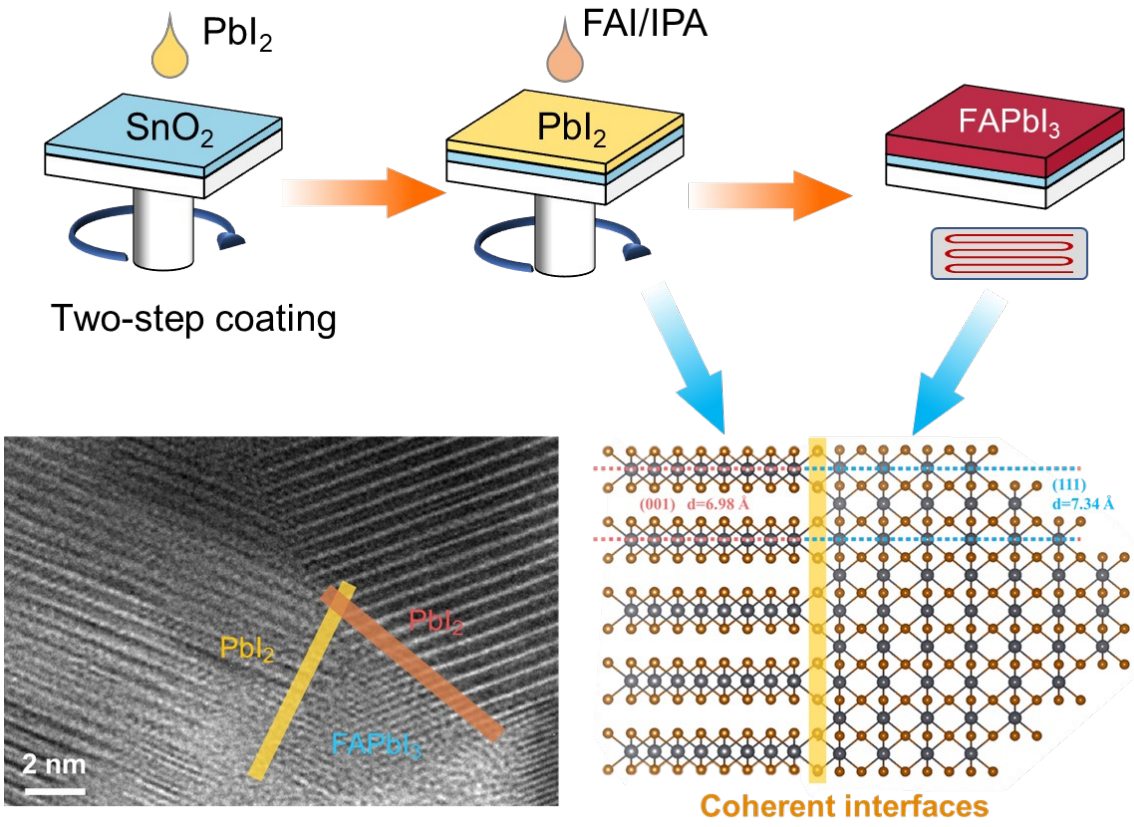

Figure S5. Schematic diagram of the two-step process for perovskite films and corresponding TEM images. The Schematic diagrams show the topochemical transformation pathway from $(001)_{PbI2}$ to $(111)_{FAPbI3}$.

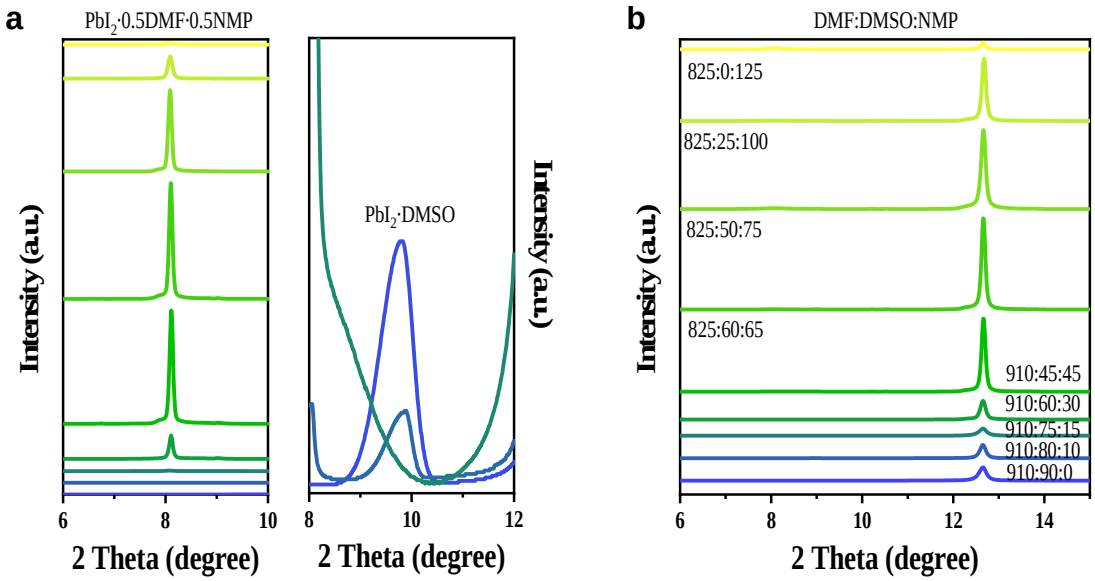

Figure S6. (a) Peak intensity variation of intermediates with different NMP content, (b) Peak intensity variation of PbI_2 films with different NMP content.

PbI_2·0.5DMF·0.5NMP intermediate phase can disrupt the chemical bonds of PbI_2·DMSO, promoting PbI_2 crystallization and making it easier for amine cations to embed into the PbI_2 octahedra, forming stable perovskite. Compared to the strong interaction between DMSO and PbI_2, the bonding interaction of NMP is weaker. Therefore, the XRD pattern shows that the PbI_2·DMSO adduct peaks are weak and broad, whereas the peaks of PbI_2·0.5DMF·0.5NMP are strong and narrow, indicating better crystallinity of PbI_2·0.5DMF·0.5NMP. The competition between the two intermediates eventually removes the PbI_2·DMSO adduct, and the well-crystallized PbI_2·0.5DMF·0.5NMP can as a template, promoting the conversion to highly crystalline PbI_2.

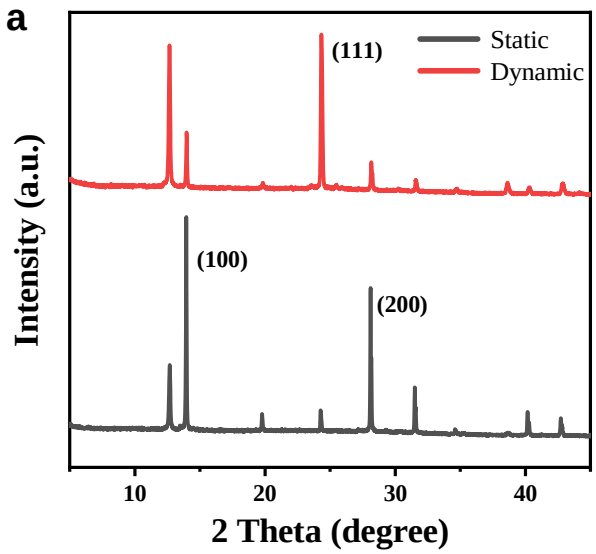
a
(111)
Static
Dynamic
(100)
(200)
Intensity (a.u.)
10
20
30
40
2 Theta (degree)

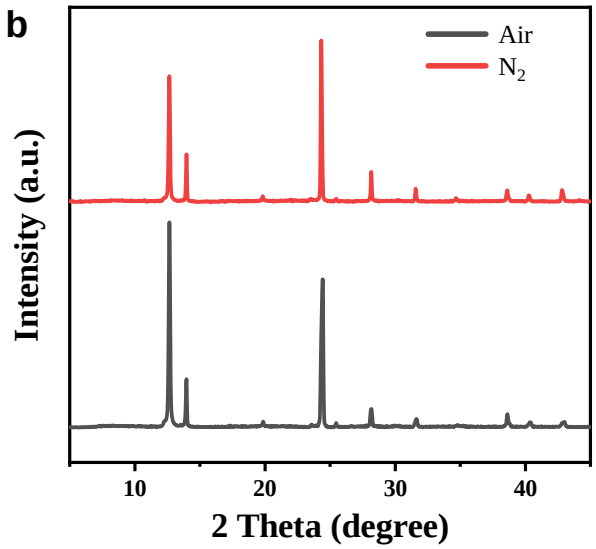
b
Air
N2
Intensity (a.u.)
10
20
30
40
2 Theta (degree)

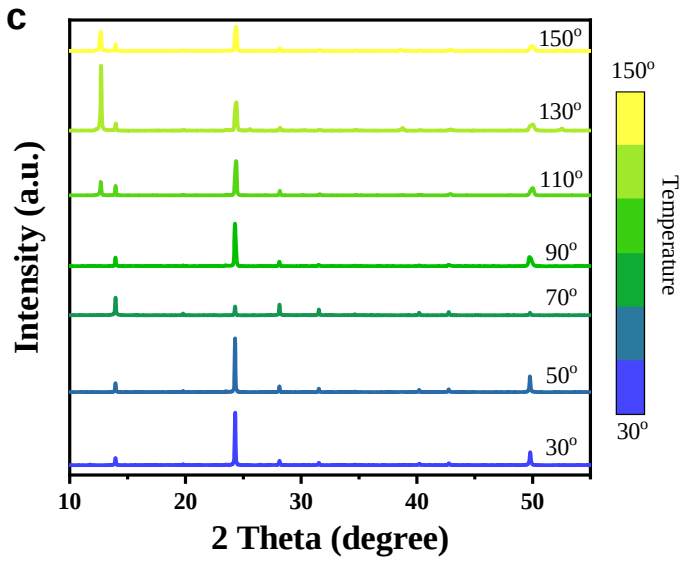
c
150°
130°
110°
90°
70°
50°
30°
Temperature
Intensity (a.u.)
10
20
30
40
50
2 Theta (degree)

Figure S7. Operational conditions influencing the orientation of perovskite films: (a) Dynamic spin-coating vs. static spin-coating when adding FAI in the second step, (b) N_2 vs. air annealing environment after the second step, (c) annealing temperature. Operational conditions also affect orientation.

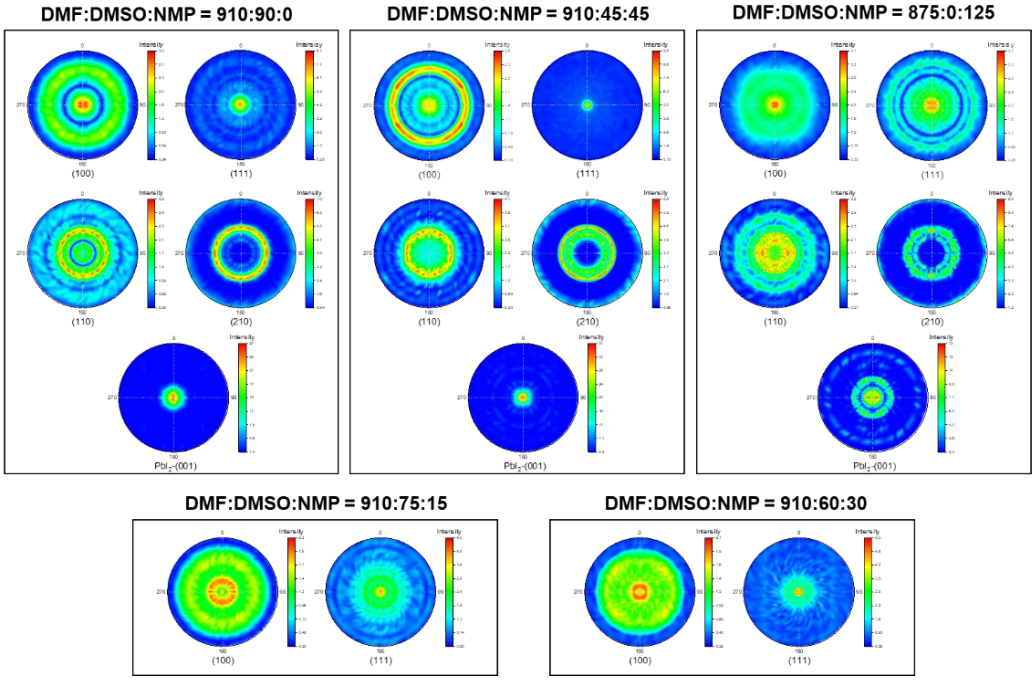

Figure S8. Pole figures of thin films in the different solvents.

The (100), (111), (110), and (210) pole figures were for perovskite phase, while (001) pole figures were for PbI_2 phase. When the max value is 1.000, the film is interpreted as being randomly oriented. When the max value exceeds 1.000, a higher value indicates a more dominant corresponding facet.

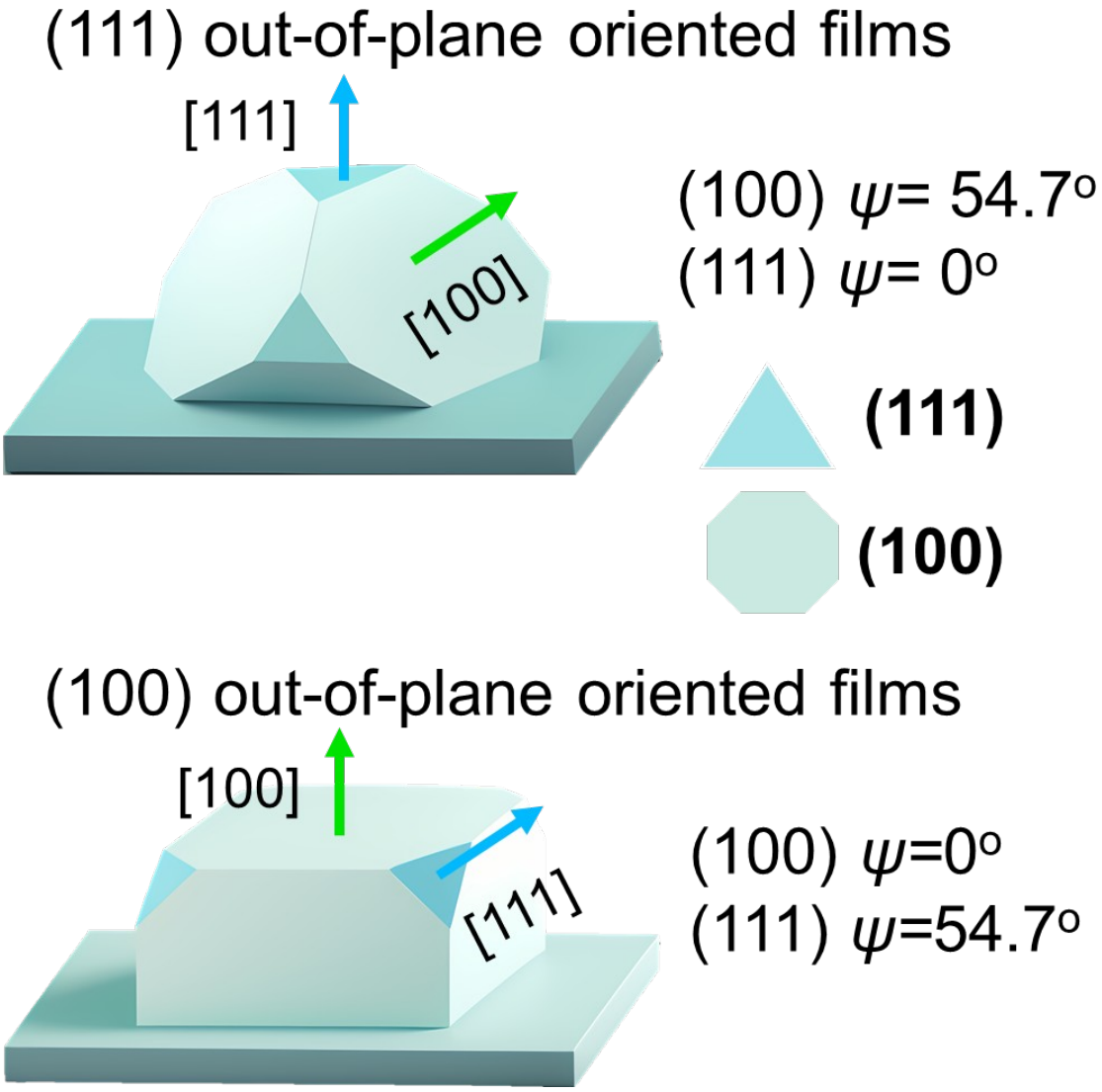

Figure S9. The schematic examples of a (111) and (100) out-of-plane oriented films.

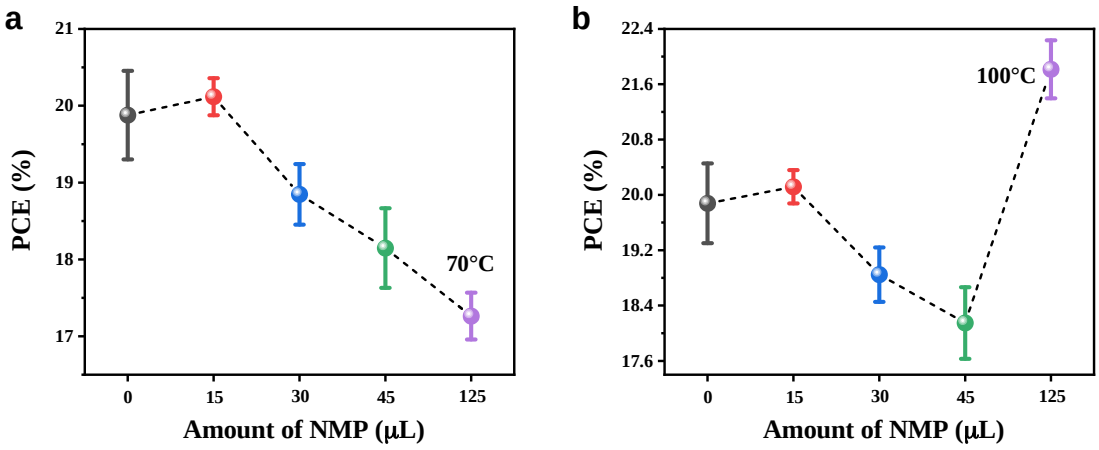

Figure S10. (a) PCE distribution of PSCs at the temperature of 70°C for PbI_2 film. (b) PCE distribution of PSCs at the temperature of 100°C for PbI_2 film with DMF/NMP solvents only. It should be noted that the annealing temperature for the PbI_2 film is 70°C. However, for the DMF/NMP system, an annealing temperature of 100°C for PbI_2 film is more appropriate, as the NMP has a higher boiling point.

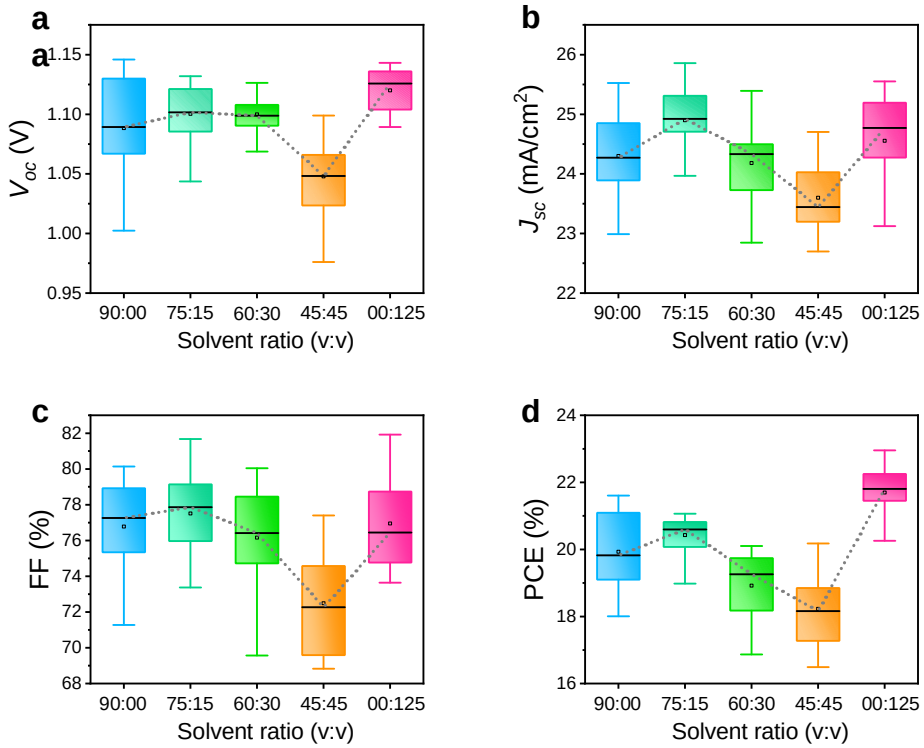

Figure S11. Box charts of (a) V_{oc}, (b) J_{sc}, (c) FF, (d) PCE with different solvent ratio, respectively.

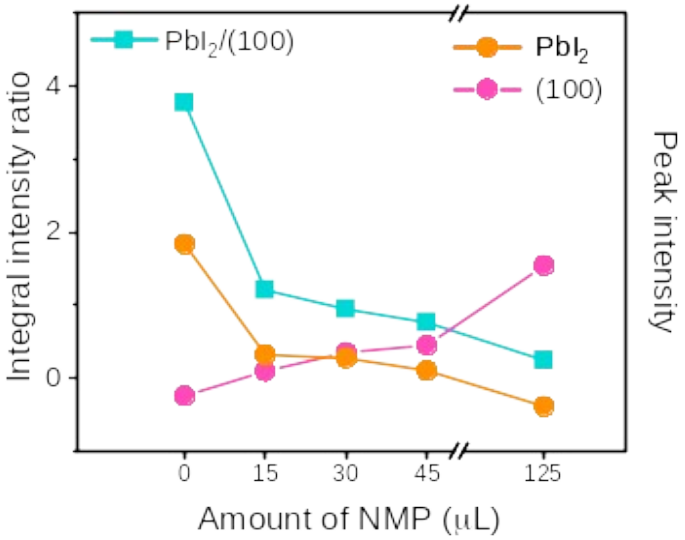

Figure S12. Integral intensity ratios of PbI_2/(100) in perovskite film, peak intensity of residual PbI_2 and (100) with varied NMP amounts.

The variations of residual PbI_2 and PbI_2/(100) follow a consistent trend, confirming that (100) is not dominant. An inverse correlation is observed between the intensities of residual PbI_2 and (100) facet peaks. Considering the epitaxial growth characteristics of (111) facets with PbI_2, this trend reflects the competitive relationship between (111) and (100) orientations.

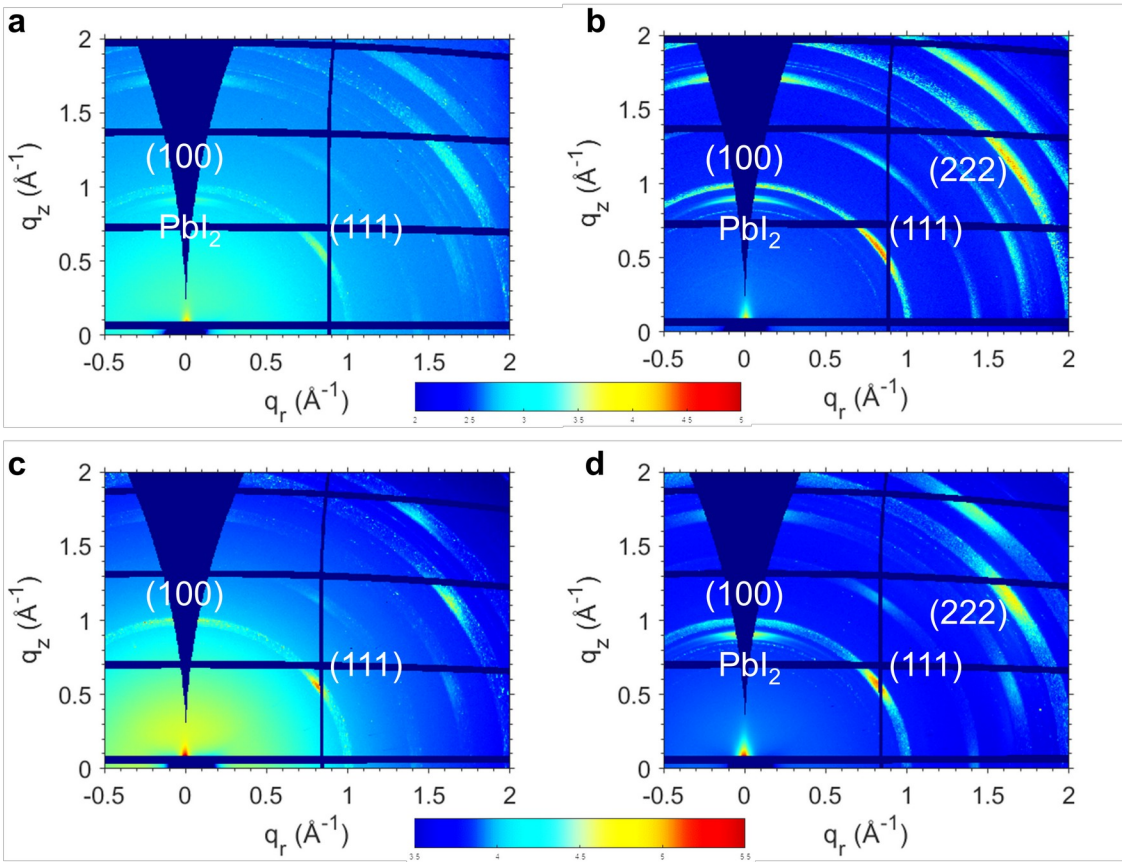

Figure S13. 2D GIWAXS patterns of control (a, b) and target (c, d) perovskite films at an incident angle of 0.6° (surface, left) and 1.2° (bulk, right), respectively.

In all samples, typical diffraction patterns of perovskite films are observed, with Debye-Scherrer rings corresponding to PbI_2, (100), and (111) crystal planes at scattering vectors q of 0.90, 1.00, and 1.41 $Å^{-1}$, respectively.[2] In the control sample displayed overlapping discrete Bragg scattering rings (or arcs), whereas the target perovskite showed azimuthally anisotropic scattering spots. GIWAXS analyses showed that the target sample exhibited characteristic scattering at 36° along q ≈ 1.00 $Å^{-1}$ (complementary to the interplanar angle ψ). This result indicates that the octahedra preferentially stack along the [111] direction while suppressing the (100) facet, which is consistent with previous analyses.

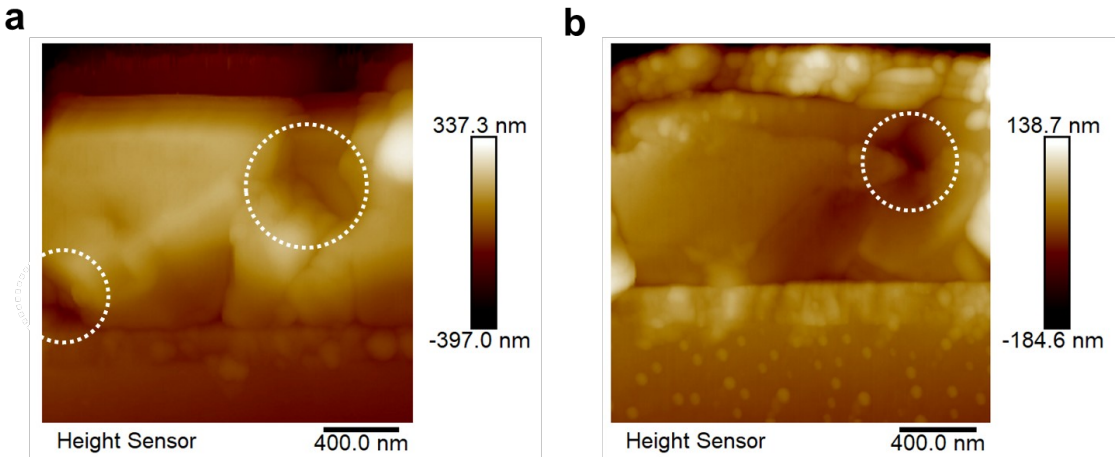

Figure S14. Cross-sectional KPFM profiling of (a) control and (b) target devices.

The control device exhibits noticeable voids caused by random orientation. In contrast, the target device primarily features deeper grain boundary (GB) vacanies resulting from misaligned heterogeneous facet orientations.

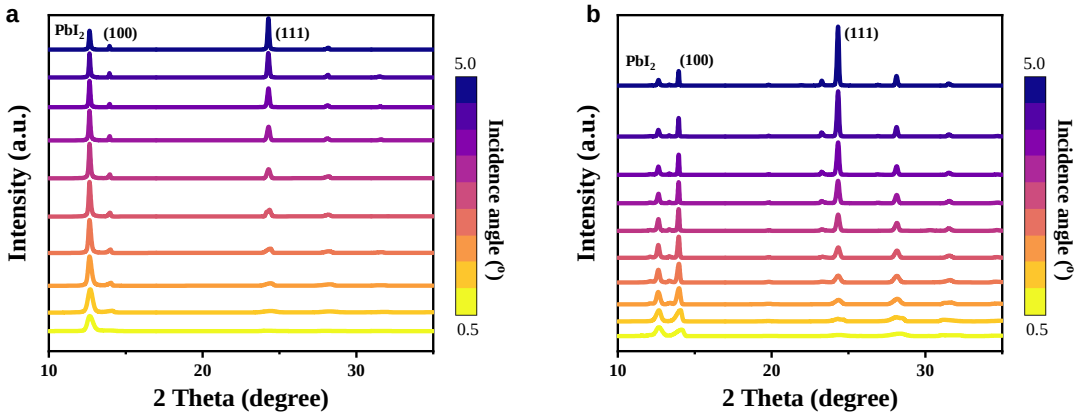

Figure S15. GIXRD pattern for the top surface of different films: (a) Control (b) Target.

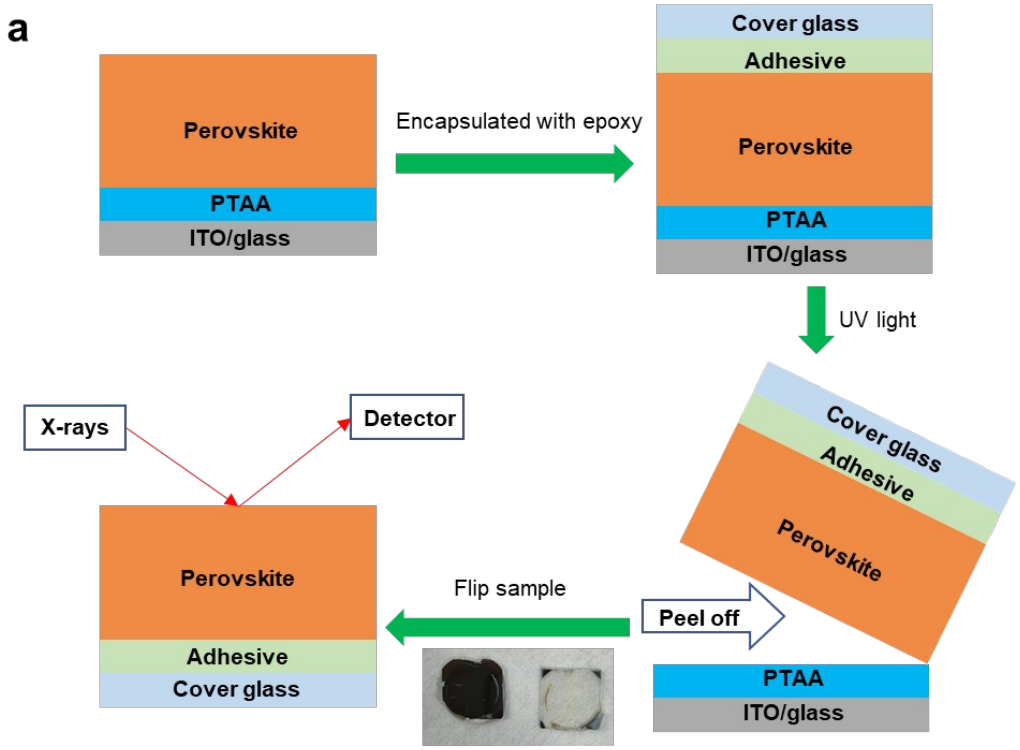

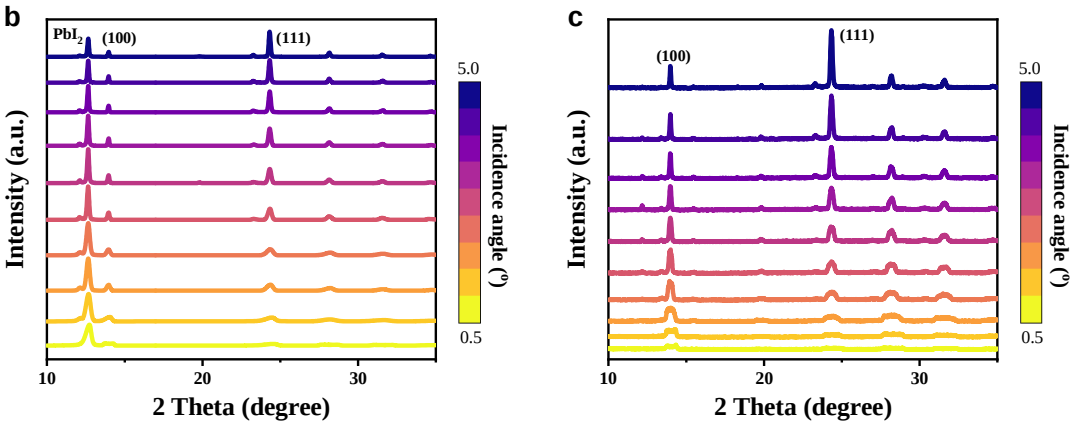

Figure S16. (a) Schematics of the preparation process for the bottom surface and the corresponding GIXRD pattern for different films, (b) Control (c) Target. The sample was prepared by peeling off the film from PTAA-covered ITO glass substrates using an adhesive epoxy sealant.

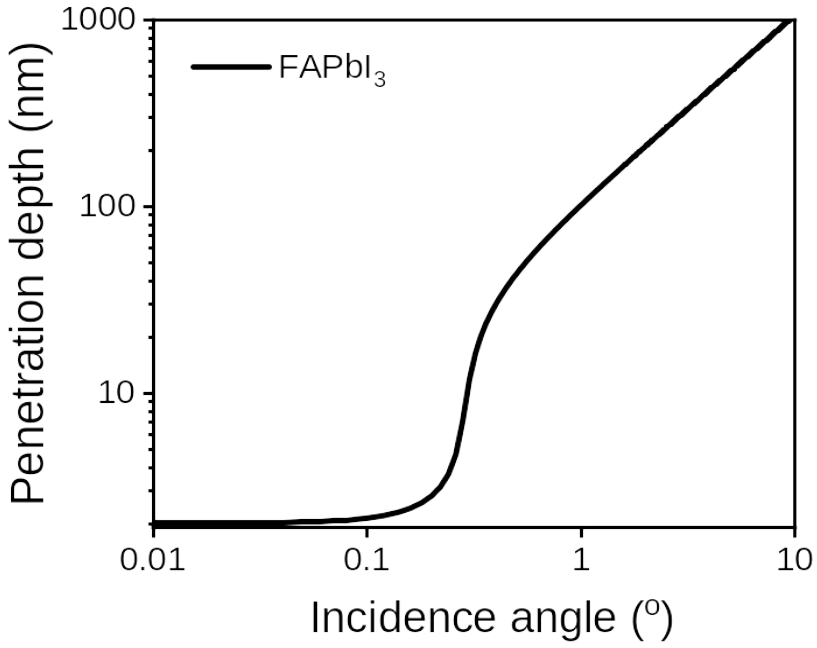

Figure S17. The GIXRD penetration depth as a function of incident angle.

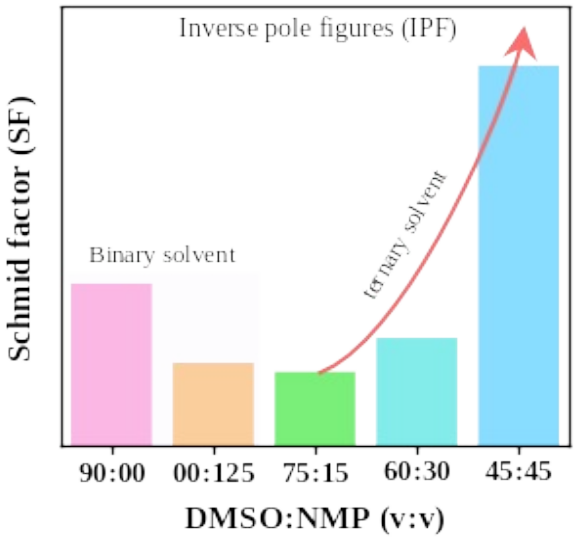

Figure S18. The schmid factor (SF) of the films with different treatments.

The vertexs of a sector represent the indices of crystal facets as projection planes. Most common IPF use the (001) plane as the projection plane, hence the indices at the sector vertex are (001). In cubic crystal systems with a symmetry of 24, any orientation will appear 24 times in a standard projection image. In an asymmetric orientation triangle composed of the vertex (001), (101) and (111), all crystal orientations can be included in the projection points only once, creating the sector of the IPF of cubic systems.[3]

From the IPF plot of ternary solvent, a preferred orientation of (111) crystal plane in the ND direction is observed, with the maximum pole density or schmid factor (SF) of ~9. The orientation of the concentrated pole points on the ND direction in the IPF are mainly (111)-dominated with

secondary (100), indicating the preferential orientation of these two facets parallel to the substrate. The projection bands perpendicular to the (111) on the TD/RD directions also confirm the primarily out-of-plane orientation of the (111) facets. Similarly, it can be concluded that DMF/DMSO solvent results in a random orientation with a higher occurrence of (111) facets, while DMF/NMP solvent leads to a random orientation with a higher occurrence of (100) facets.

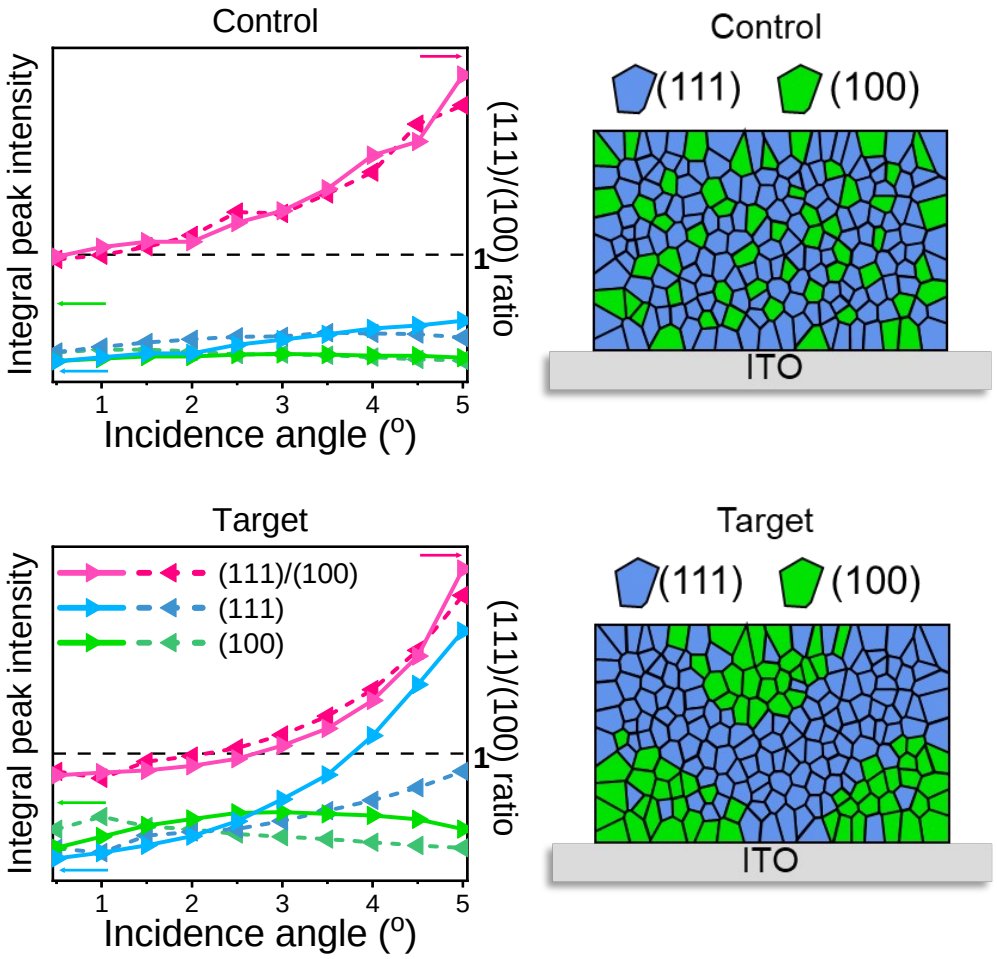

Figure S19. GIXRD patterns of surface and buried interface for the target and control films, and corresponding vertical distribution models with (100) and (111) facet.

To visualize the textured facet distribution, we further deepen our understanding by analyzing the (111)/(100) ratio. Interestingly, our results demonstrate an exponential rise in facet ratio,

indicating that with increasing penetration depth, the (111) facet gradient increases while the (100) facet gradient decreases, forming a textured structure with a top-down pyramid-like arrangement. GIXRD patterns at the bottom of the perovskite film also support these findings, although the changes are less pronounced compared to the top, suggesting that from the top surface downward, the (100) facet gradient decreases rapidly. Conversely, the proportion of (100) facets is higher at the bottom at low angles. From the bottom surface upward, the (100) facet enrichment is more significant, with a slower gradient decrease. This behavior contrasts with the random orientation observed in the control film. The ratio between the two peaks at the bottom remains consistently above 1, and the ratio shows irregular fluctuations, indicating random orientation.

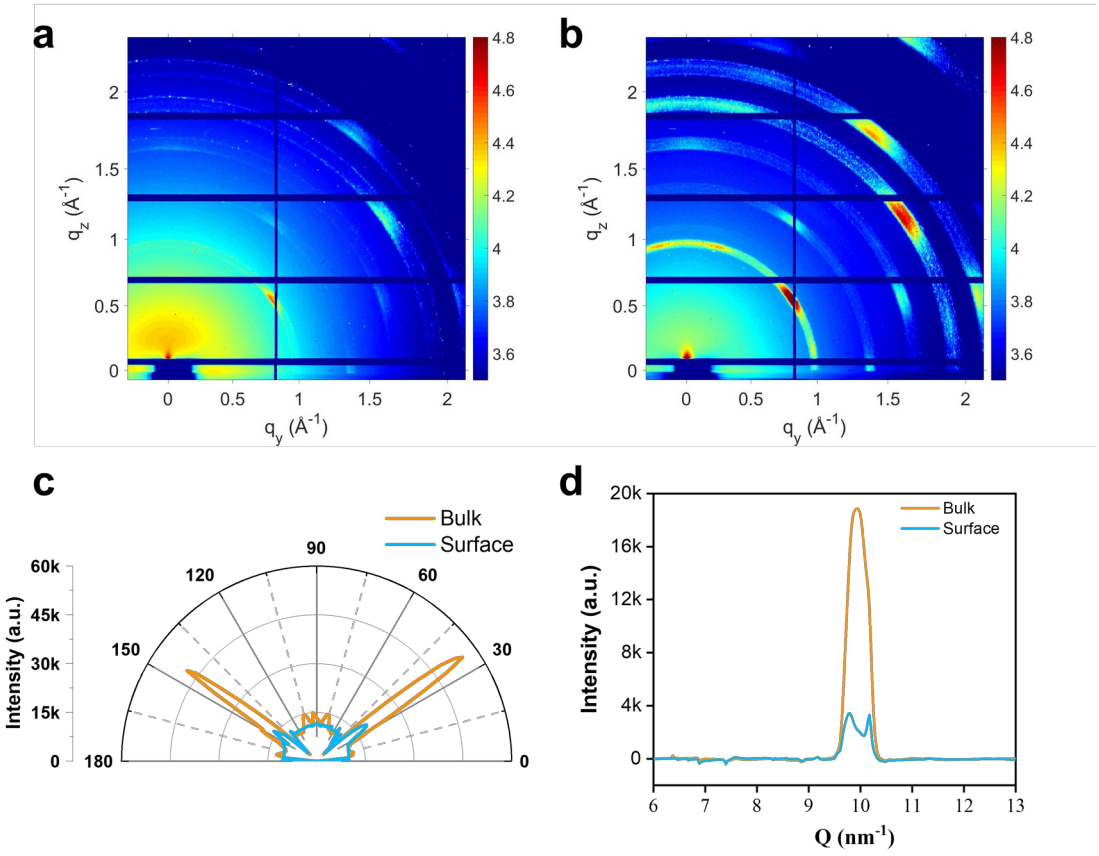

Figure S20. (a, b) 2D GIWAXS patterns of unannealed target perovskite films at an incident angle of 0.6° (surface, left) and 1.2° (bulk, right), respectively. (c) Radially integrated intensity plots along the $FAPbI_3$-(100) ring. (d) The 1D GIWAXS derived from the corresponding 2D GIWAXS patterns.

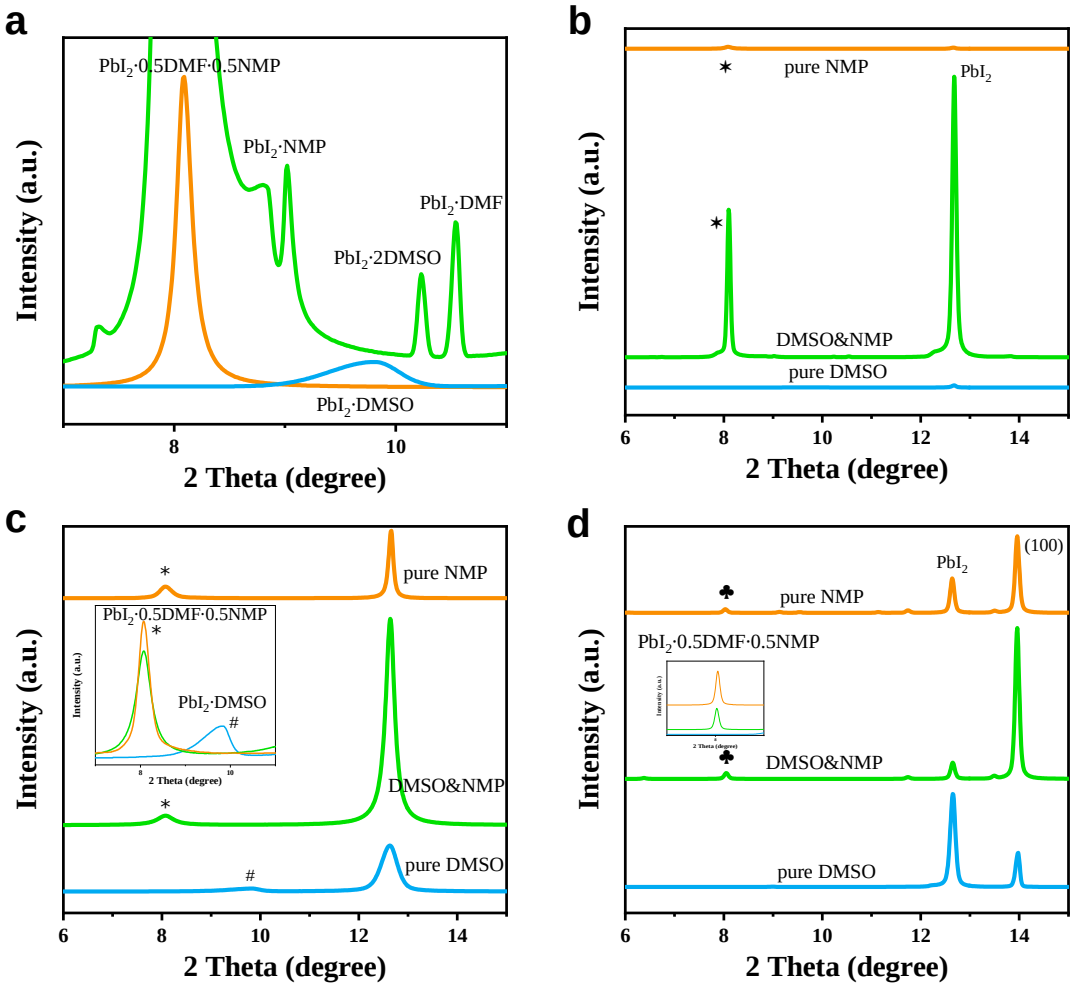

Figure S21. XRD patterns of films with different solvents under various conditions: (a,b) unannealed PbI_2 films, (c) annealed PbI_2 films, and (d) annealed perovskite films.

In the first step, the PbI_2·0.5DMF·0.5NMP peak intensity significantly surpasses that of PbI_2·DMSO, which is more apparent in the XRD patterns of unannealed films, reaching its maximum under the target condition.

Compared to the strong interaction between DMSO and PbI_2, the bonding interaction of NMP is weaker. Therefore, the XRD pattern shows that the PbI_2·DMSO adduct peaks are weak and broad, whereas the peaks of PbI_2·0.5DMF·0.5NMP are strong and narrow, indicating better crystallinity of PbI_2·0.5DMF·0.5NMP. The competition between the two intermediates eventually removes the PbI_2·DMSO adduct, and the well-crystallized PbI_2·0.5DMF·0.5NMP can as a template, promoting the conversion to highly crystalline PbI_2.

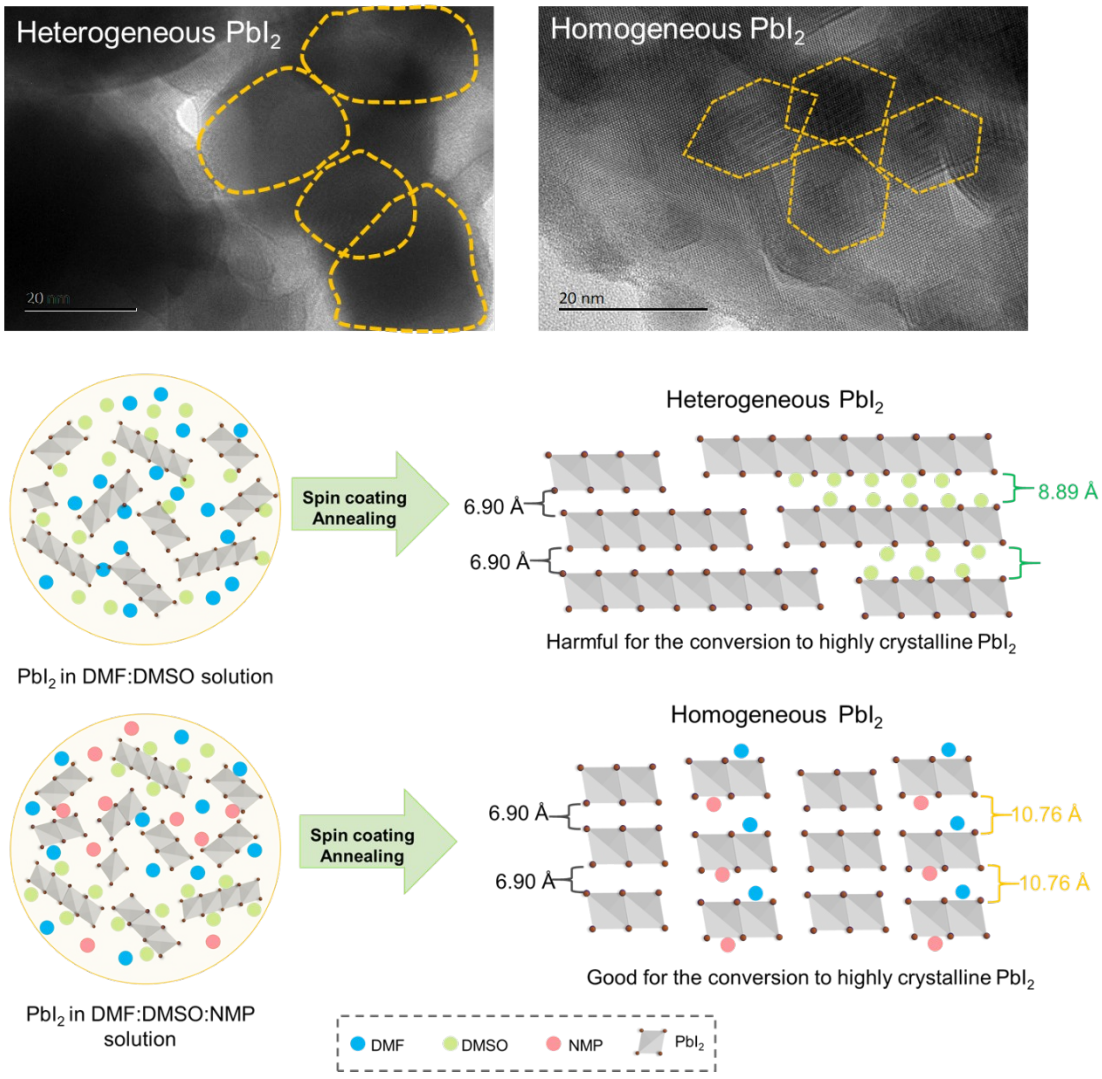

Figure S22. TEM images of heterogeneous and homogeneous PbI_2 films, and schematic diagram

of the crystallization process of PbI_2 films under different solvent environments.

TEM data illustrates that with NMP intervention, PbI_2 exhibits improved ordering and enhanced crystallinity, transforming heterogeneous PbI_2 into homogeneous PbI_2. Combined with other diffraction data, we can infer that the PbI_2·0.5DMF·0.5NMP intermediate phase serves as a growth template, promoting PbI_2 crystallization while inhibiting the growth of the original (100) facets, thereby creating favorable conditions for (111) facet formation.

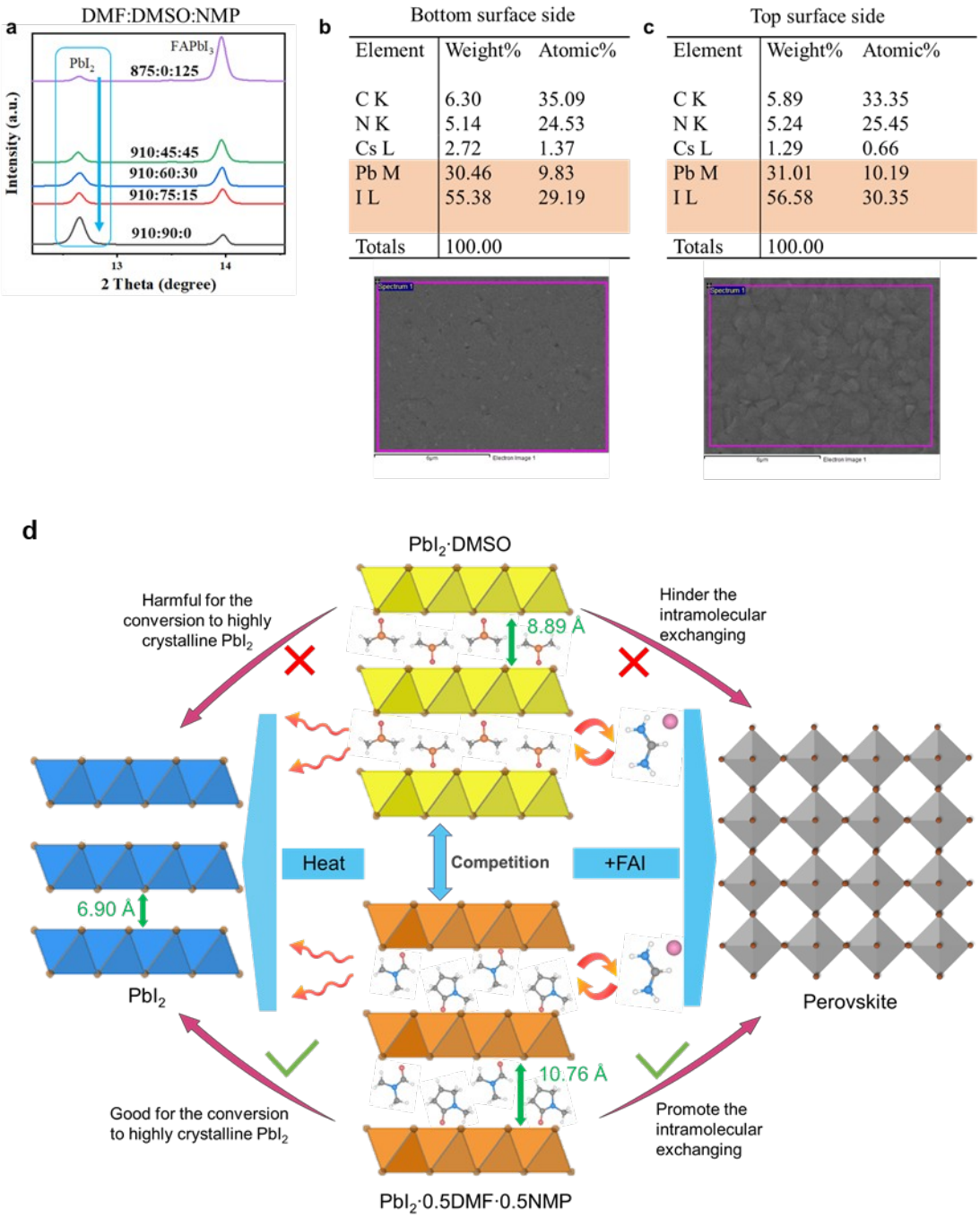

Figure S23. (a) XRD patterns of perovskite film with varied NMP amounts. (b,c) The element amount in the target film measured by EDS from both bottom and top surface. (d) The schematic diagram of the competitive mechanisms involved.

Previous data have thoroughly discussed the competitive conversion mechanism between PbI_2·0.5DMF·0.5NMP and PbI_2·DMSO intermediates in their transformation into PbI_2. Here, additional insights into the competition between these two intermediates during perovskite formation are provided. A ternary system is more effective in suppressing an excessive amount of

lead iodide. The residue of PbI_2·DMSO adduct hinders the incorporation of amine cations into the PbI_2 lattice. Additionally, according to previous work,[4] compared to DMSO, the interaction between NMP and ammonium salts is stronger,[5] leading to a larger spacing in the PbI_2 framework of PbI_2·0.5DMF·0.5NMP. This accelerates the intramolecular exchange, promoting the insertion of ammonium cations into the PbI_2 framework and forming stable perovskite.

However, kinetically, this process suppresses (111) facet growth. And the strong affinity between FAI and NMP provides more nucleation sites for perovskite growth, favoring the formation of the thermodynamically preferred low-surface-energy (100) facet. This explains the exist of the non-dominant (100) facet in the films. In contrast, the DMF/DMSO binary system does not encounter this issue. The residual PbI_2·DMSO adduct hinders the incorporation of amine cations into the PbI_2 lattice. However, this results in final films that are less compact and contain more voids.

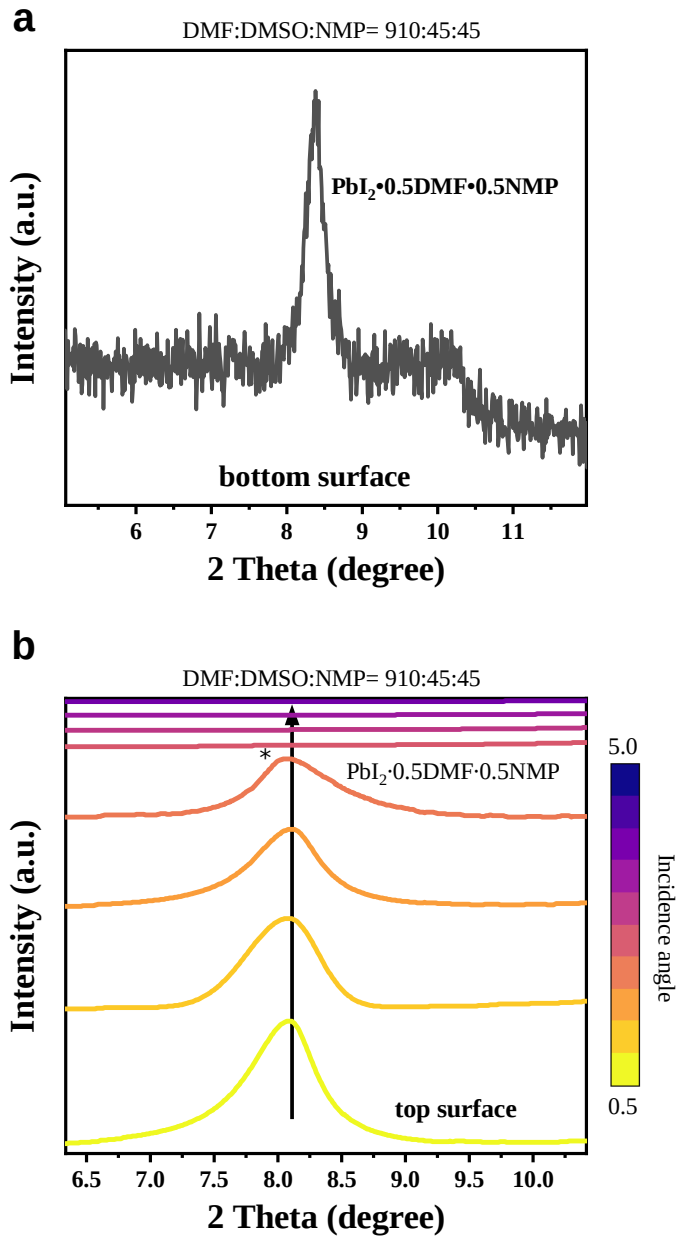
a
DMF:DMSO:NMP= 910:45:45
Intensity (a.u.)
PbI2•0.5DMF•0.5NMP
bottom surface
6
7
8
9
10
11
2 Theta (degree)
b
DMF:DMSO:NMP= 910:45:45
Intensity (a.u.)
*
PbI2·0.5DMF·0.5NMP
top surface
5.0
0.5
Incidence angle
6.5
7.0
7.5
8.0
8.5
9.0
9.5
10.0
2 Theta (degree)
c
DMF:DMSO:NMP= 910:45:45
Intensity (a.u.)
top surface
bottom surface
(100)
PbI2
δ
♣
PbI2·0.5DMF·0.5NMP
10
20
30
2 Theta (degree)

Figure S24. (a) XRD patterns of PbI_2 film at the bottom surfaces with target condition. (b) GIXRD patterns of PbI_2 film at the top surfaces with target condition. (c) XRD patterns of the bottom and top surfaces for target perovskite film.

This also explains why the (100) facet gradient is concentrated on both the top and bottom surfaces in ternary solvents system: a portion of NMP intermediates becomes embedded at the bottom, preventing evaporation, while another portion remains on the surface due to its high boiling point, not fully volatilizing. Ultimately, the NMP intermediate phase induces an intermediate phase that favors the (100) orientation. It can be observed that intermediates are still buried at the bottom of the perovskite films.

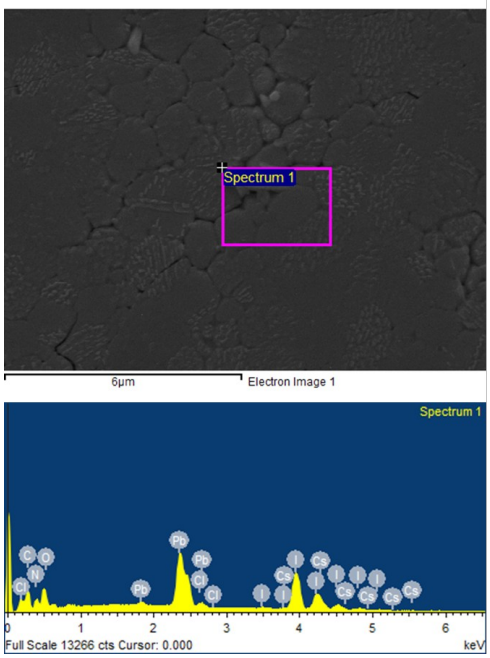

DMF:DMSO:NMP=910:45:45

Element	Weight%	Atomic%
C K	4.67	27.73
N K	4.37	22.25
Cs L	2.29	1.23
Cl K	0.63	1.27
O K	1.31	5.84
Pb M	32.29	11.11
I L	54.43	30.58
Totals	100.00	

Figure S25. The element amount of a certain area in the target film measured by EDS from the bottom surface.

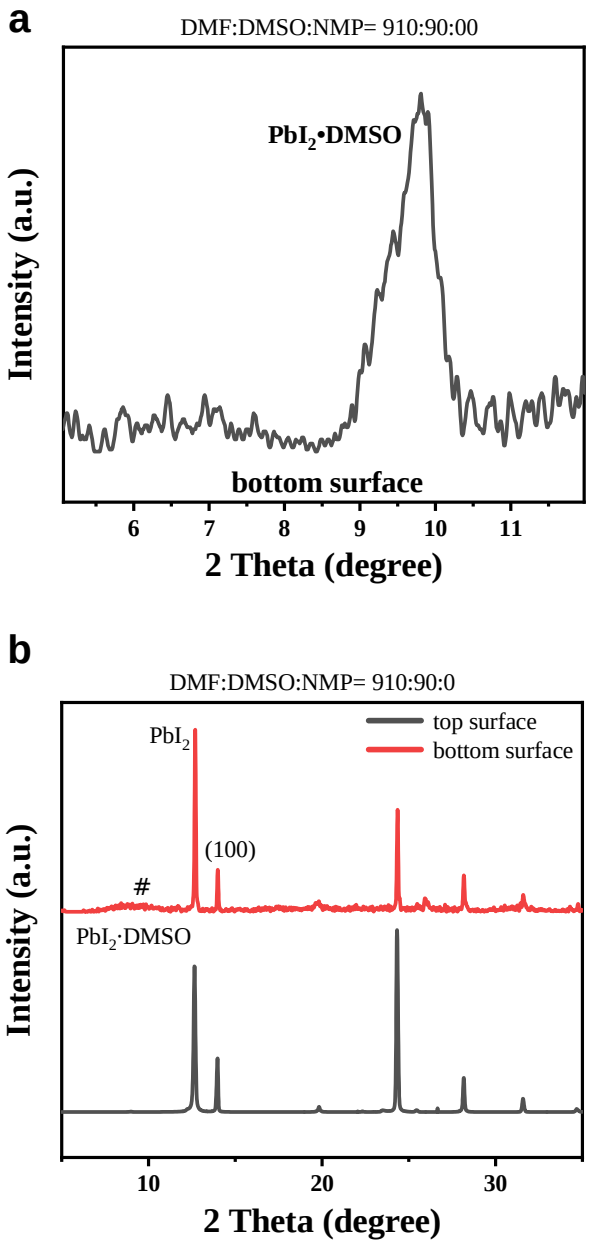

Figure S26. (a) XRD patterns of PbI_2 film at the bottom surfaces with control condition. (b) XRD patterns of perovskite film at the bottom and top surfaces with control condition.

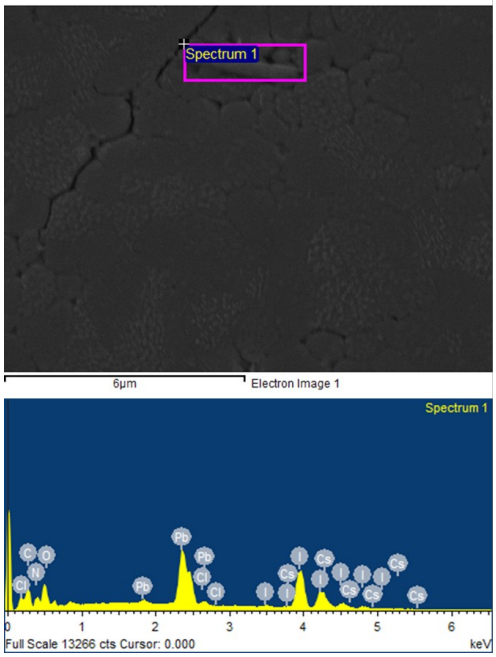

DMF:DMSO:NMP=910:90:00

Element	Weight%	Atomic%
C K	4.60	27.43
N K	4.34	22.19
Cs L	2.23	1.20
Cl K	0.53	1.07
O K	1.35	6.04
Pb M	32.13	11.11
I L	54.82	30.95
Totals	100.00	

Figure S27. The element amount of a certain area in the control film measured by EDS from the bottom surface.

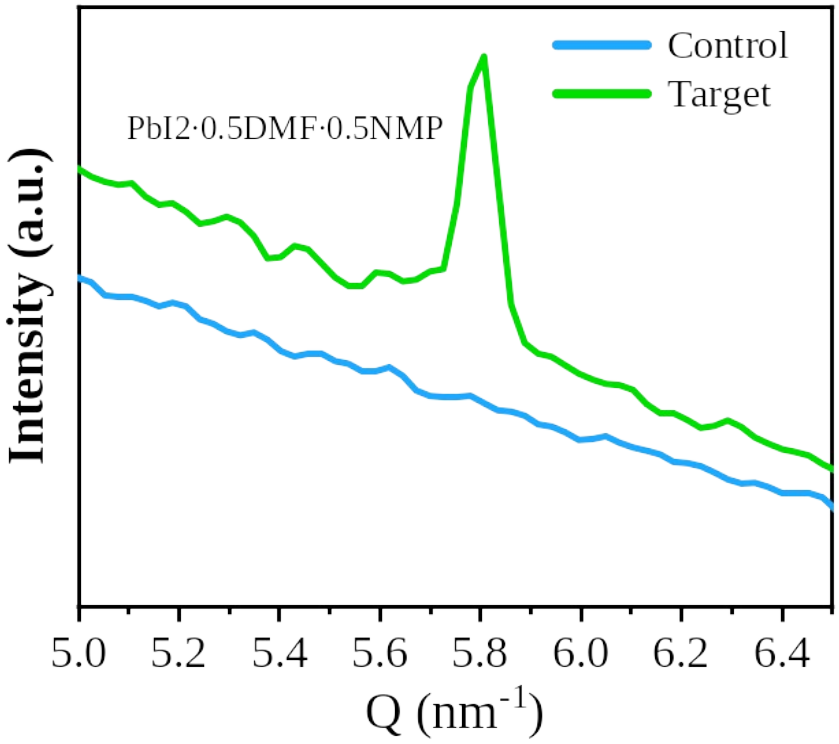

Figure S28. Derived 1D-GIWAXS spectra of intermediate phase in perovskite films.

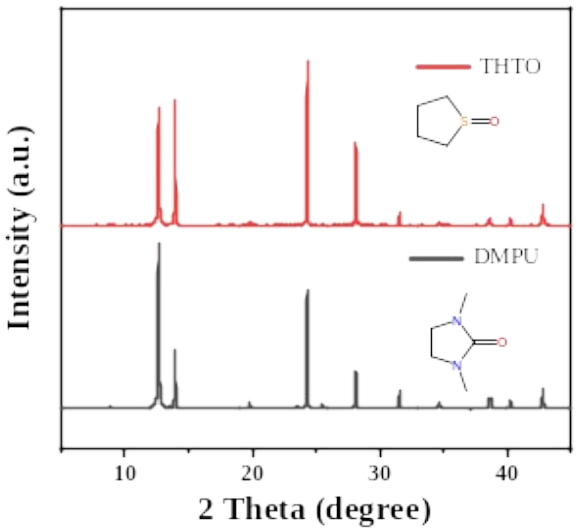

Figure S29. XRD patterns of with different solvents replacing NMP, such as tetrahydrothiophene oxide (THTO), and dimethylpropyleneurea (DMPU).

Comparatively, other solvents do not exhibit the significant effects of NMP, likely due to the intermediate phase formed by NMP.

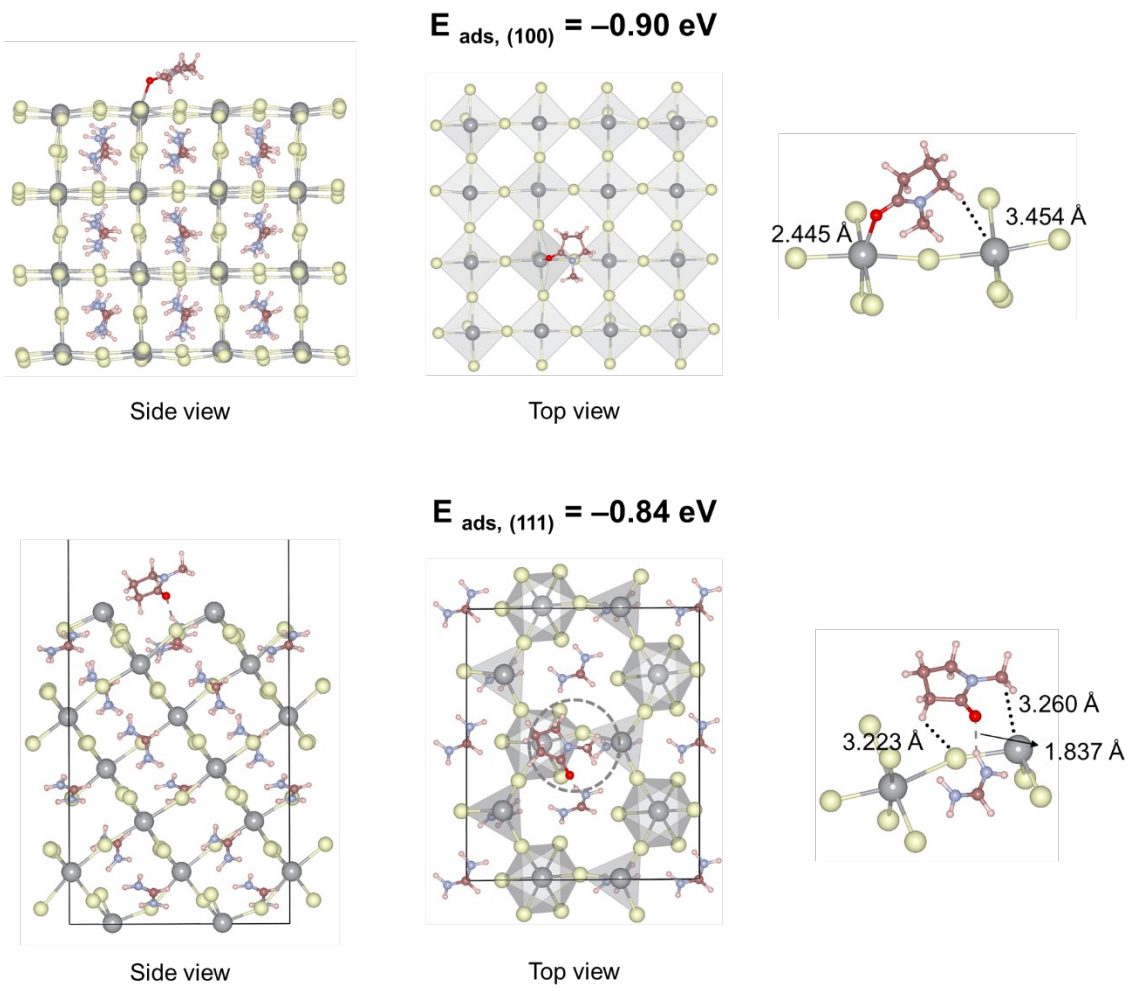

Figure S30. Calculated models of NMP adsorbed on (100) and (111) facets of $FAPbI_3$ and the corresponding adsorption energies (E_{ads}).

To expose the (111) facet—which inherently has a higher surface energy—the common approach is to introduce additives that lower the surface energy, making the facet energetically favorable. In our study, as we transition from a binary to a ternary solvent regulation strategy, the additive introduced is the NMP molecule. By placing NMP molecules on the perovskite's (100) and (111) surfaces, we calculated the adsorption energies (Eads). The results show that | Eads, (111)| < | Eads, (100)|, indicating that NMP tends to adsorb more on the (100) facet, as illustrated in Figure R9. Due to the electrostatic interactions provided by NMP—including hydrogen bonding and covalent interactions—as well as steric hindrance, its selective adsorption lowers the surface energy of the (100) facet. This, in turn, slows the growth of the (100) facet, ultimately favoring the (100) orientation. However, these DFT results conflict with our experimental observations,

demonstrating that the (111) orientation in the two-step process is governed more by kinetic factors rather than by thermodynamic control.

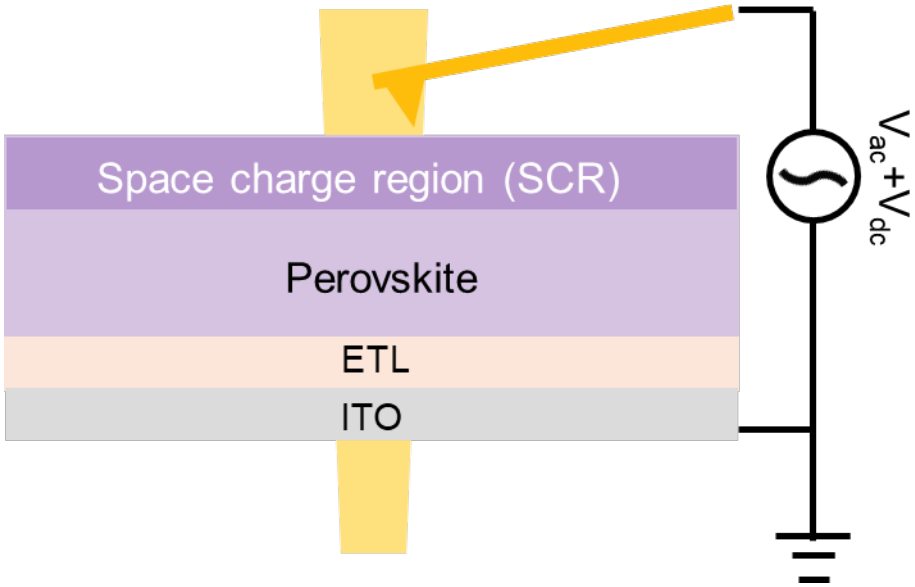

Figure S31. Schematic of energy band diagram measured in dark or under illumination.

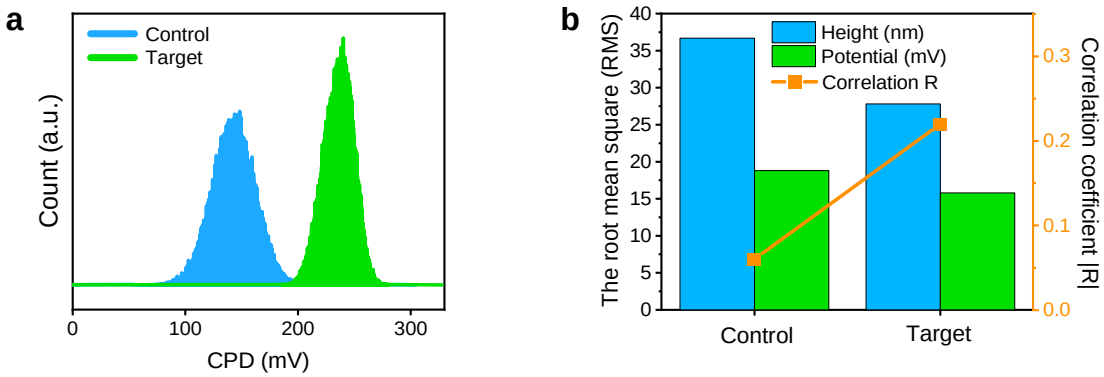

Figure S32. (a) The distribution of CPD for Figure. 4E-4H. (b) The root mean square (RMS) of height and CPD mappings (left axis) and correlation coefficient R between height and CPD mappings (right axis).

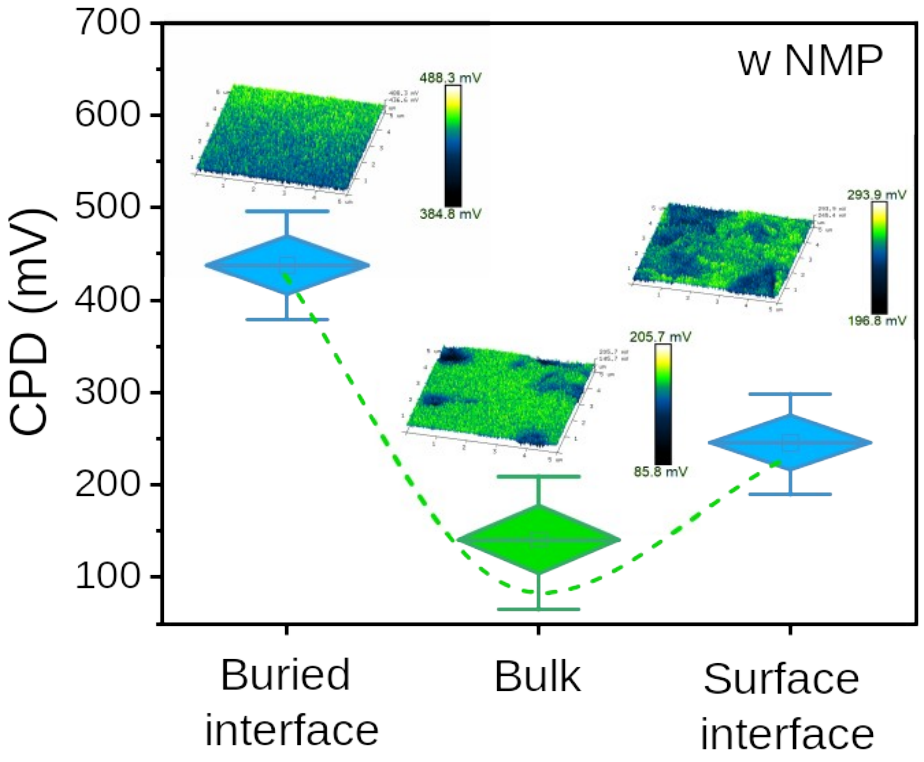

Figure S33. The CPD values between the surface and buried interface of the target film compared to the bulk.

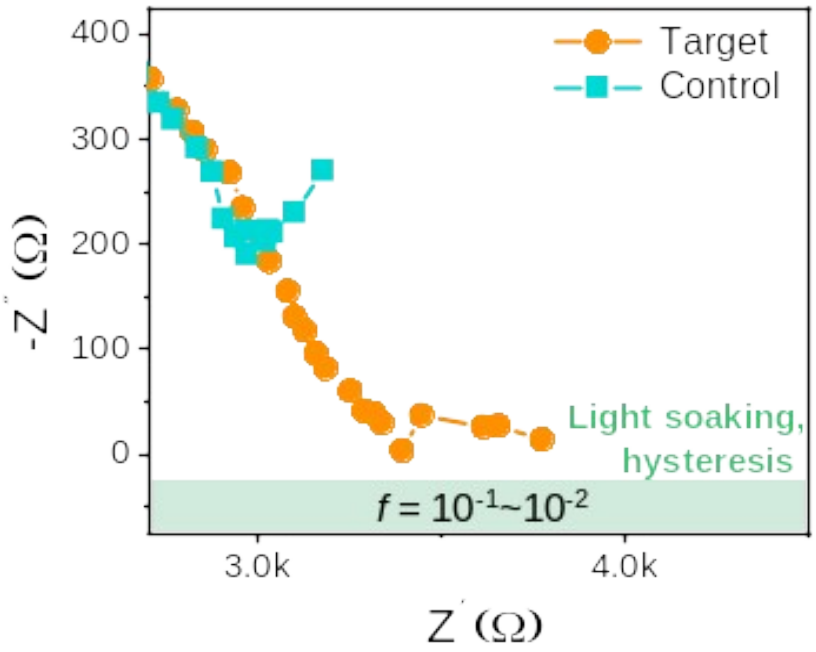

Figure S34. The enlarged Nyquist plots for Figure. 5C.

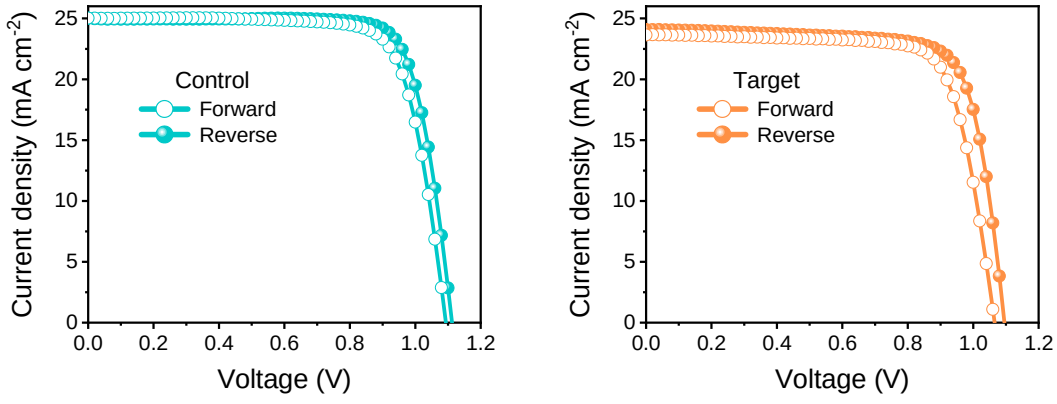

Figure S35. *J-V* curves under forward and reverse scanning with different conditions.

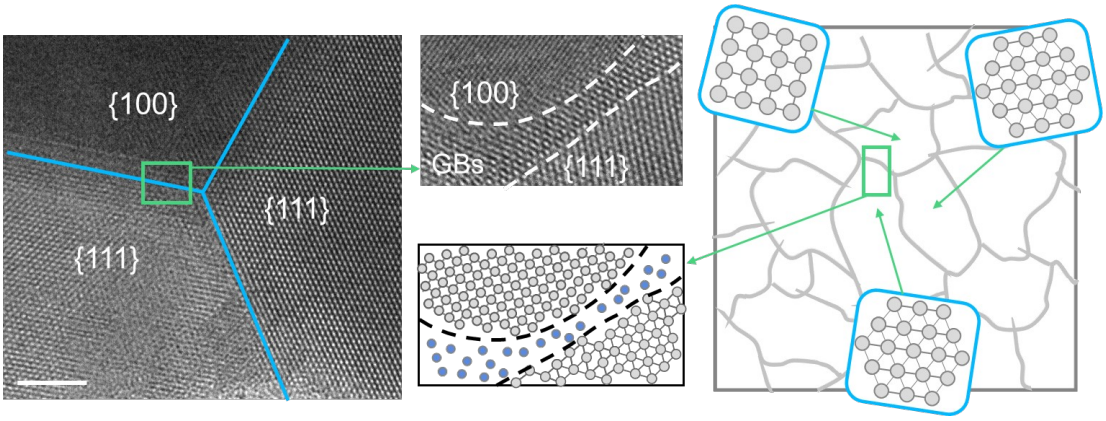

Figure S36. TEM images and schematics of the GBs defects, inset scale bars: 5 nm.

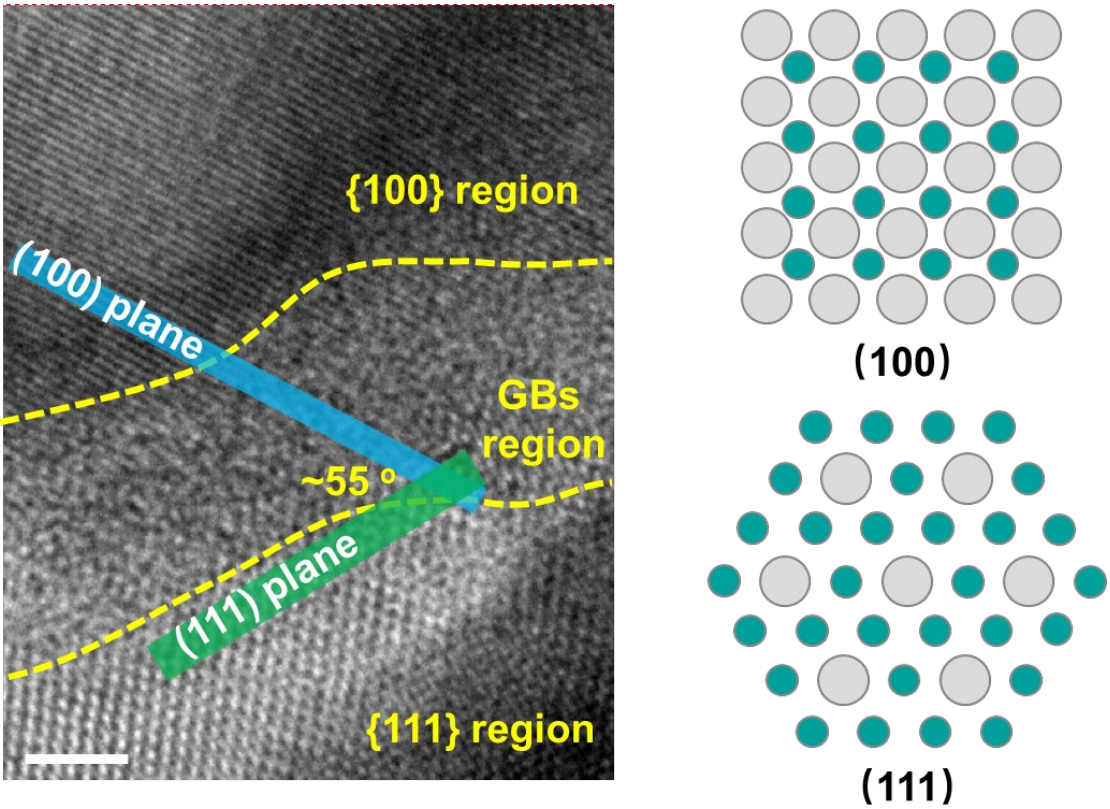

Figure S37. TEM images and schematics of the (100) and (111) facets, inset scale bars: 5 nm.

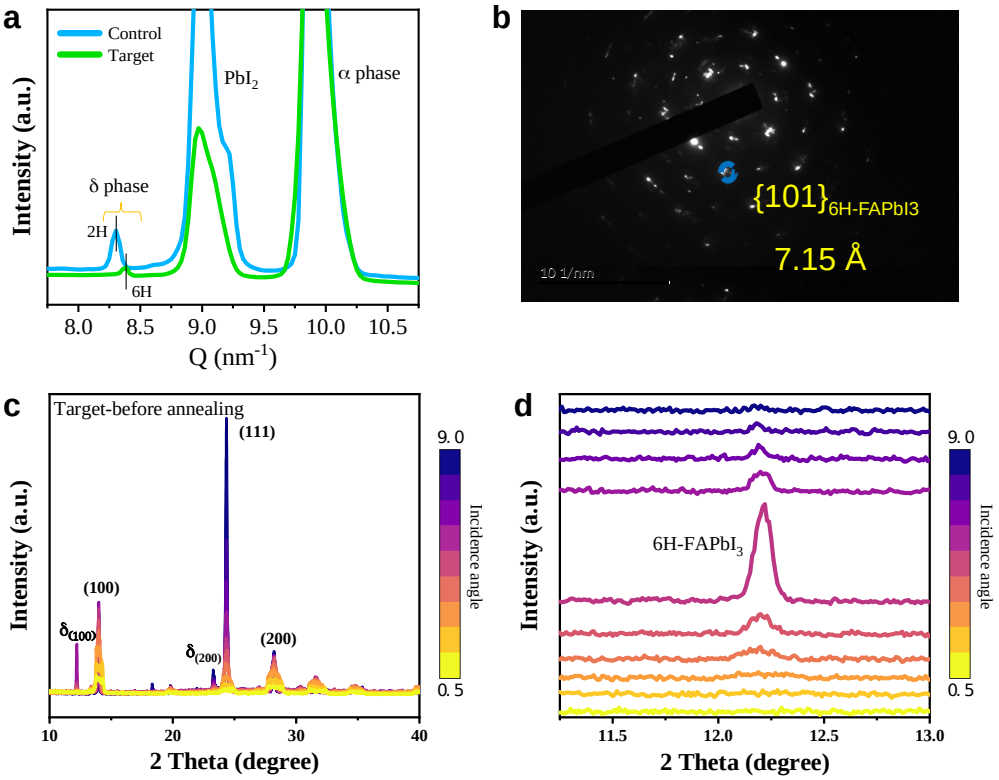

Figure S38. (a) Derived 1D-GIXRD spectra of different yellow phases. (b) The SAED pattern of target sample, scale bar: 10 1/nm. A distance 7.15 Å was derived from SAED pattern, which is consist with (001) of 6H-$FAPbI_3$.[6] (c-d) GIXRD measurements and detailed enlarged views of the target films before annealing.

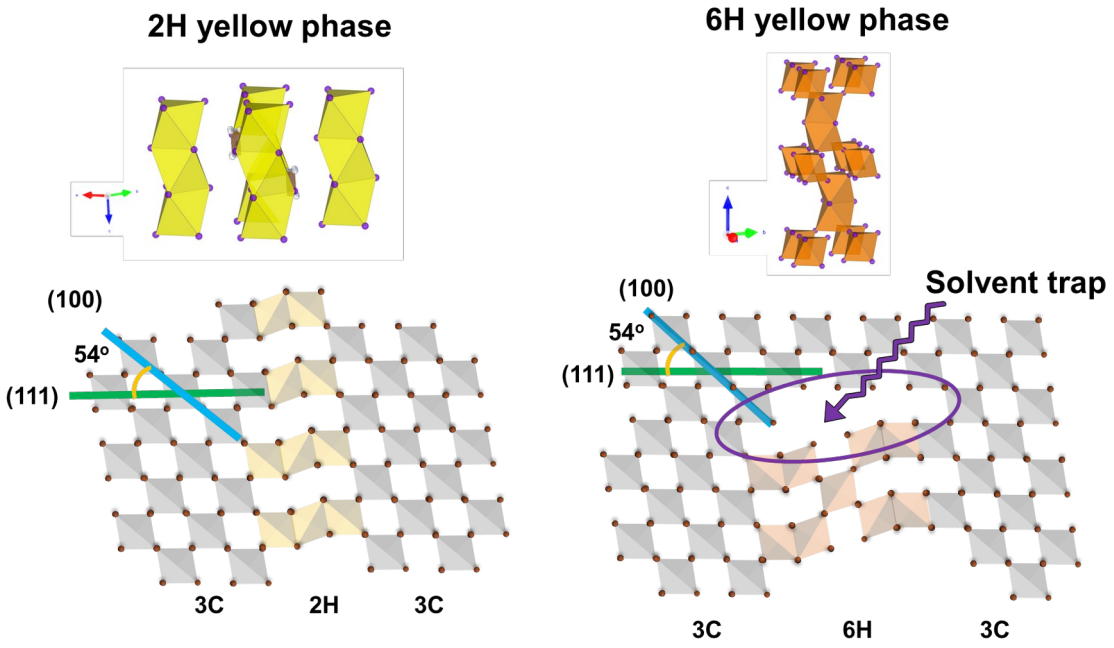

Figure S39. The schematics of 2H and 6H phases, along with their corresponding coherent lattice structures at the interfaces.

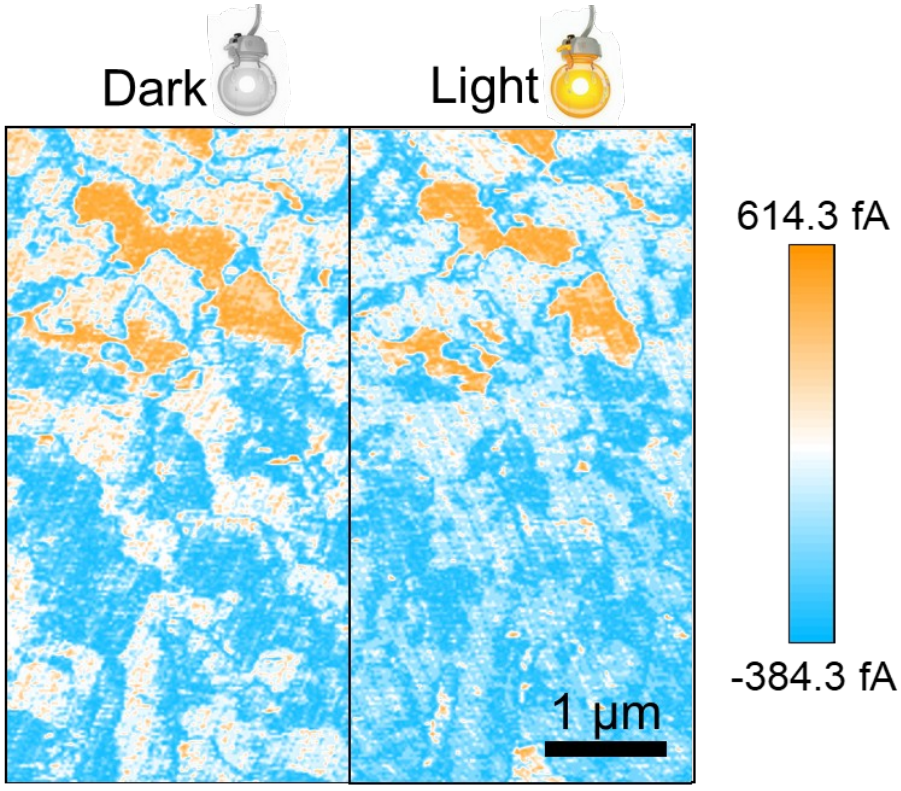

Figure S40. c-AFM images of the target film.

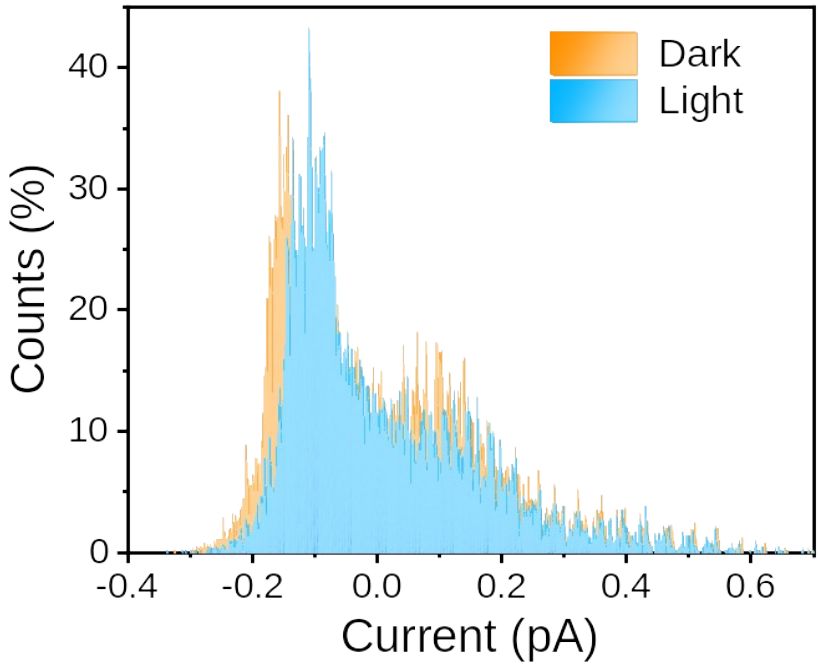

Figure S41. The current distribution in the c-AFM images.

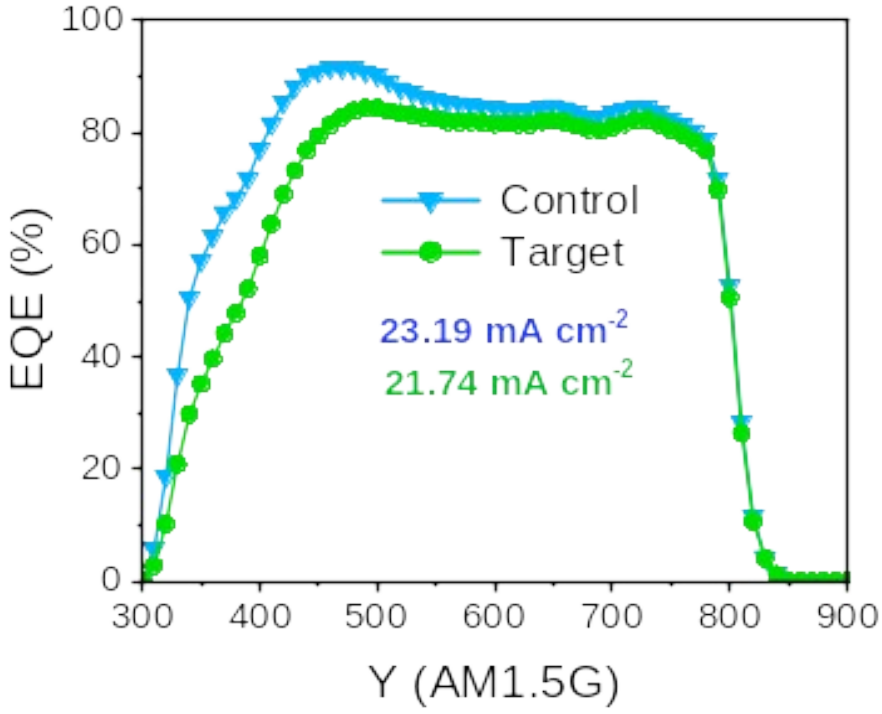

Figure S42. The EQE spectrum and integrated J_{SC} of control and target devices.

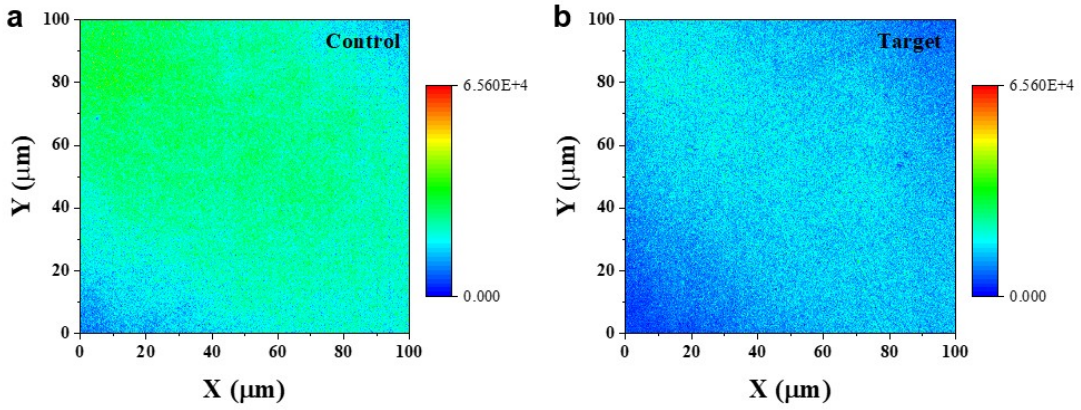

Figure S43. PL mapping of (a) control and (b) target films.

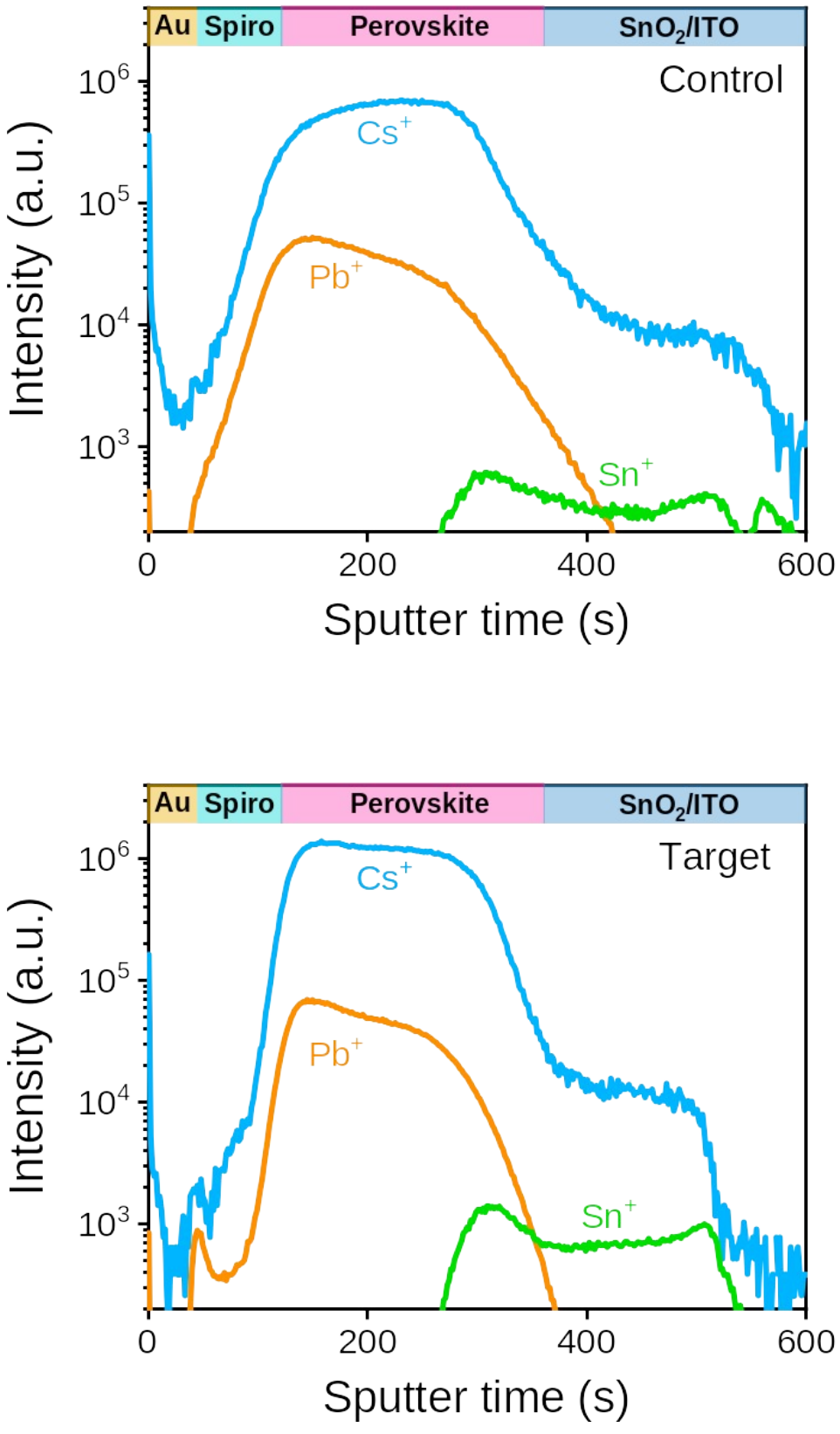

Figure S44. TOF-SIMS depth profiles of the control and target PSCs.

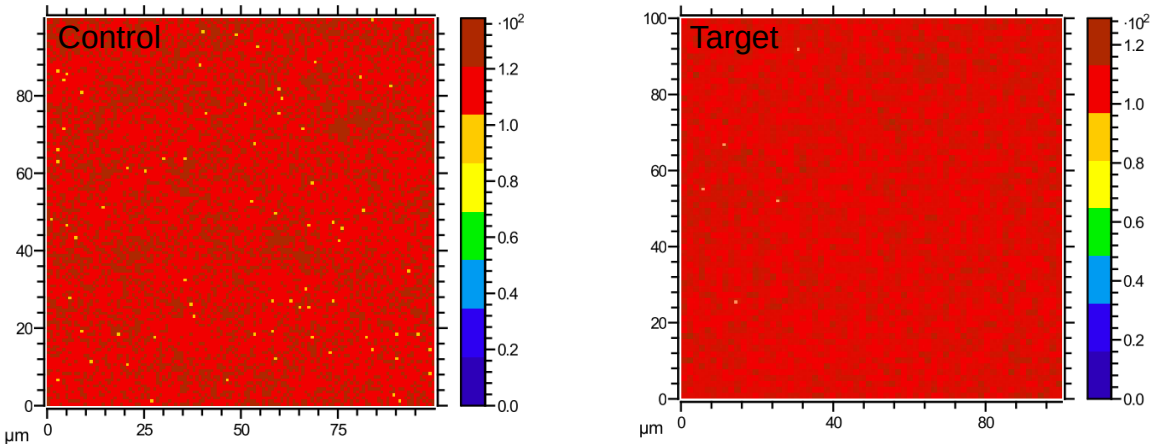

Figure S45. 2D TOF-SIMS mapping for the control and target PSCs of the initial states.

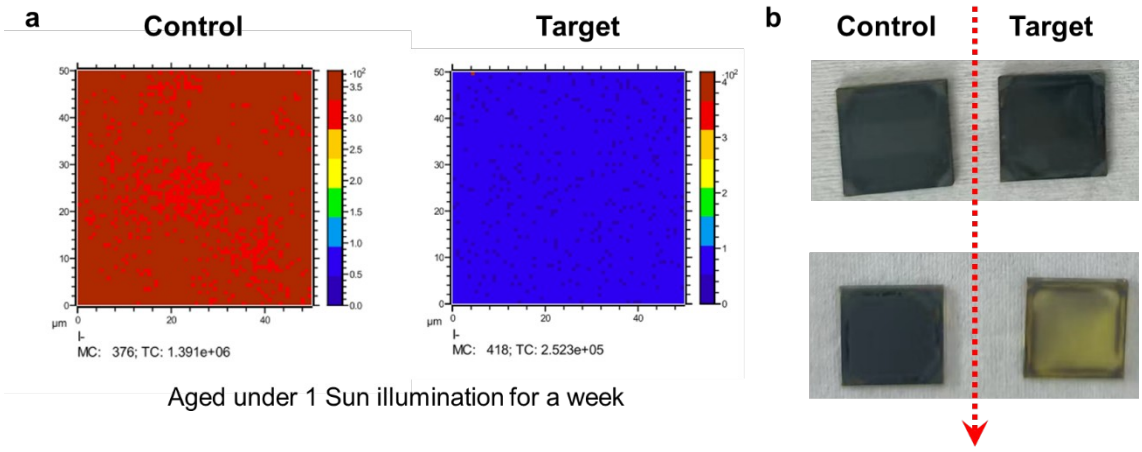

Figure S46. (a) 2D TOF-SIMS mapping of I^- of different perovskite devices aged under 1 Sun illumination for a week and (b) the corresponding photo images of the initial and final states.

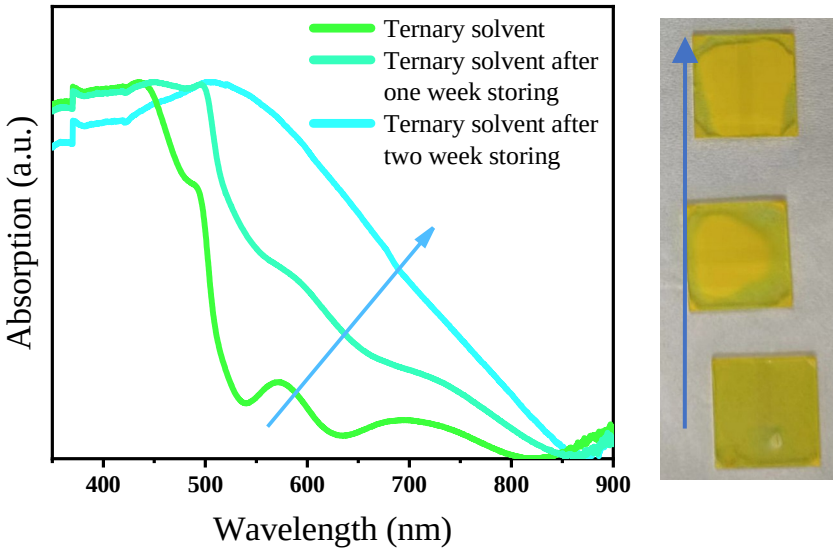

Figure S47. The UV-vis absorption spectra of aged target PbI_2 films.

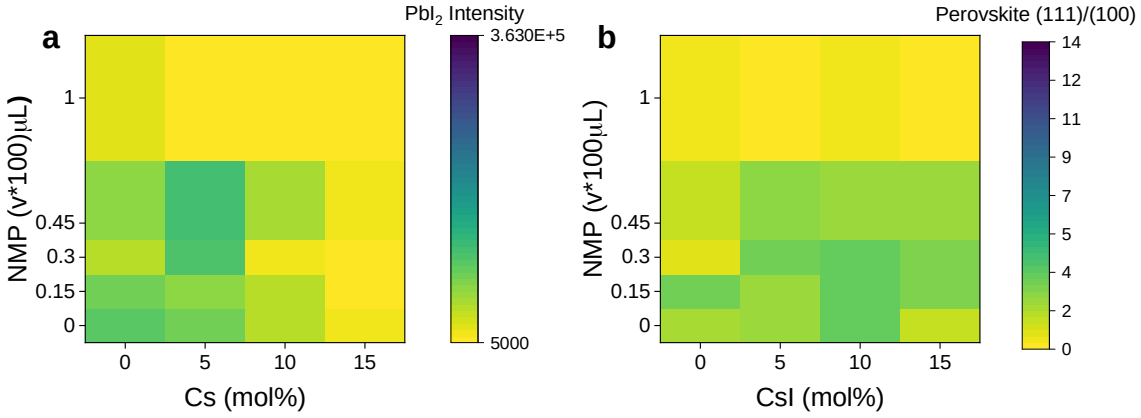

Figure S48. (a,b) Binary diagrams for XRD pattern of films spin-coated from aged lead iodide and perovskite solutions after one week.

The aged films show no clear rule of change, indicating that the more mixed elements present, the more pronounced the turbidity. Specifically, we utilized the integral intensity ratio over (111)/(100) as an orientation indicator. Low values (ratio<1.5) suggest (100) orientation, high values (ratio>3) suggest pure (111) orientation, and 1.5<ratio<3 suggest mixture of (111) and (001) orientation.

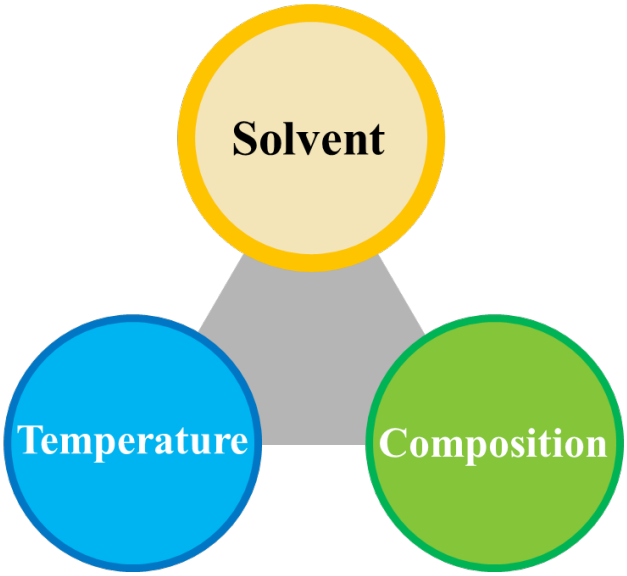

Figure S49. Several factors related to the two-step method can impact orientation, primarily summarized as three factors: solvent, composition and temperature. The facet-related issues induced by solvents in the target can also be adjusted through the other two factors.

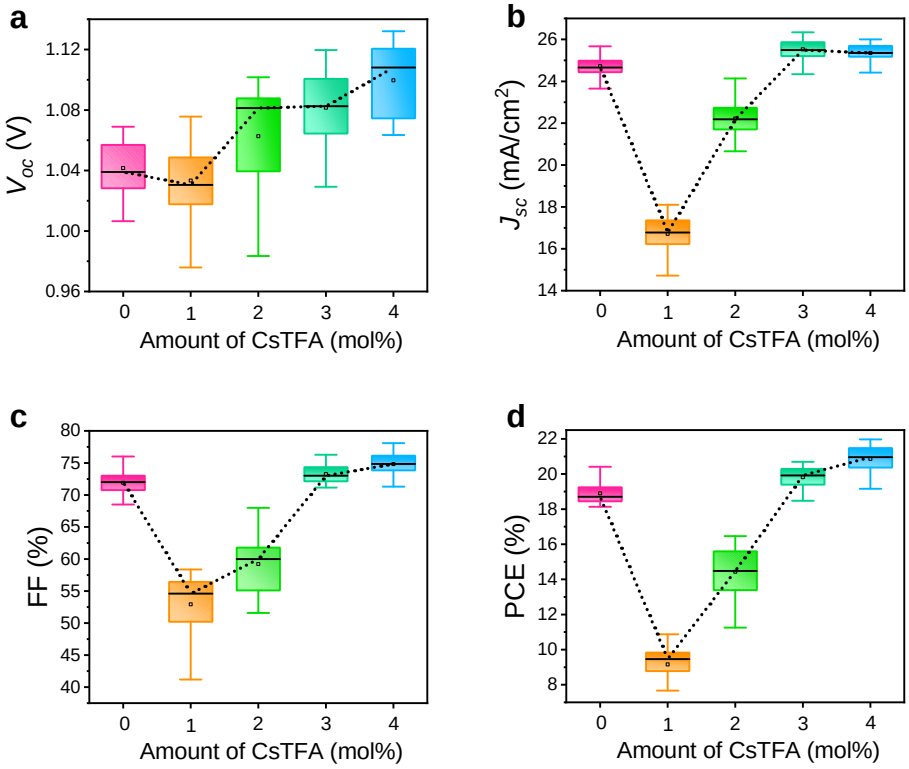

Figure S50. Box charts of (a) Voc, (b) Jsc, (c) FF, (d) PCE with different amount of CsTFA modification, respectively.

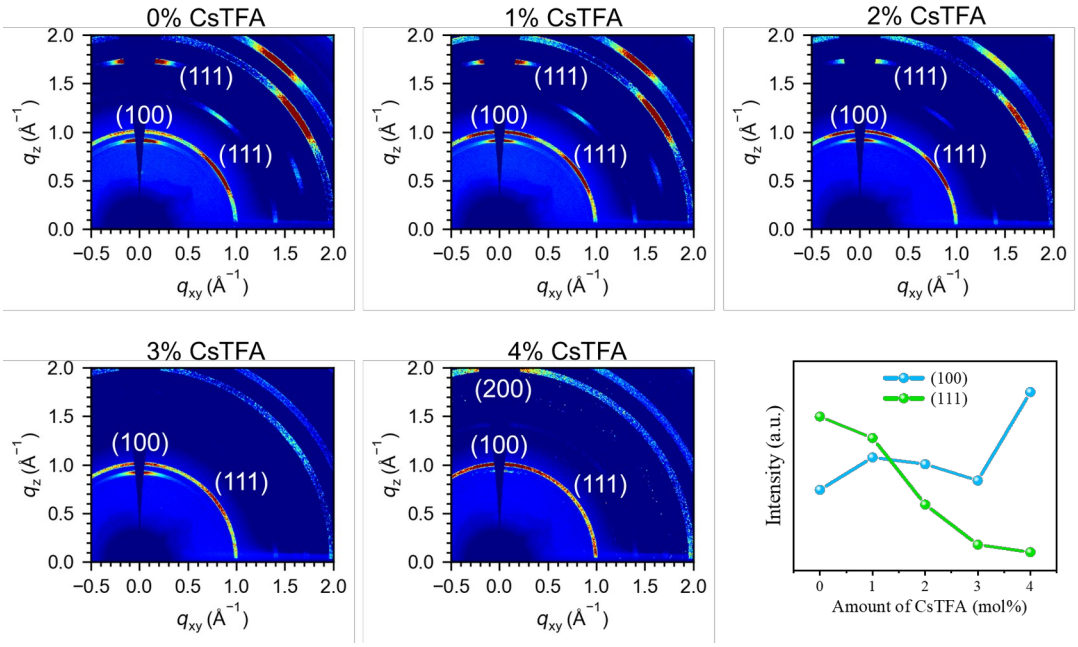

Figure S51. 2D GIWAXS patterns in target condition with different additive amount and their corresponding peak intensity obtained from the (111) facets and (001) facets.

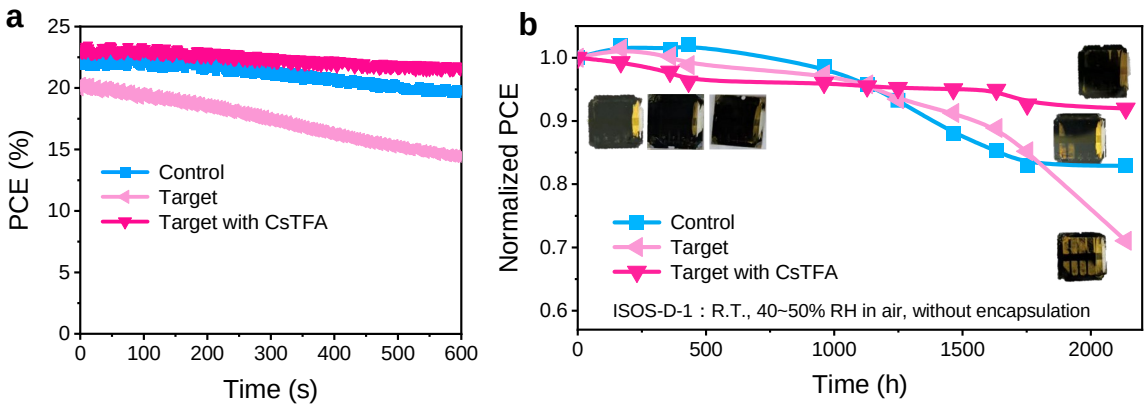

Figure S52. (a) Steady-state power output (SPO) of the solar cells for 600 s. (b) Long-term stability test under a RH of 40%-50% at room temperature (ISOS-D-1) and photos of the initial and final states.

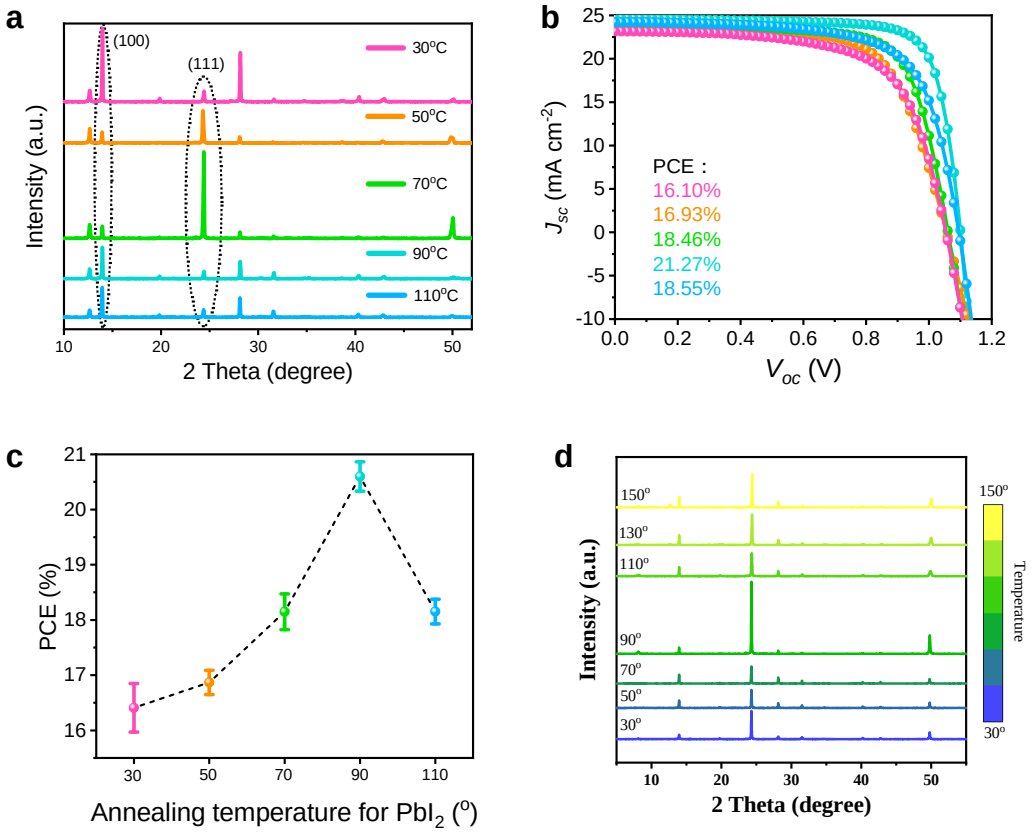

Figure S53. (a-b) XRD patterns in target condition with different annealing temperature for the first step and their corresponding PCEs. (c) PCE distribution of PSCs. (d) XRD patterns in target condition with different annealing temperature for the second step.

Changes in annealing temperature can also address solvent-induced issues. For instance, the optimal annealing temperature for DMSO is 70°C, while for NMP, it is 100°C. Thus, adjusting the temperature to accommodate mixed-solvent systems is a viable approach. As shown in Figure. 6E and 6F, an annealing temperature of 90°C yielded the highest efficiency (~21%). This adjustment specifically targets the annealing temperature of the first-step PbI_2 layer. In contrast, the annealing temperature of the second step has a minimal impact on orientation, primarily affecting crystallization intensity (Figure. S13). This indirectly demonstrates that the texture distribution of facets is closely related to the solvent system.

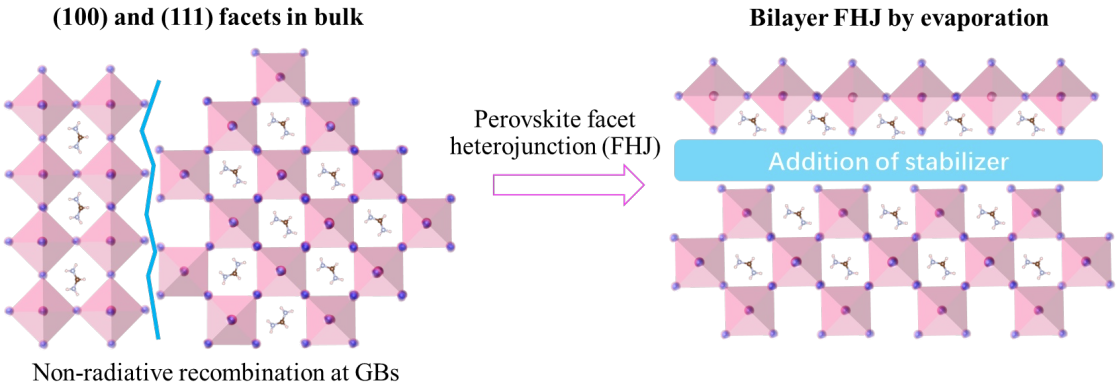

Figure S54. Schematic illustration of the design route of the perovskite facet heterojunction (FHJ).

Currently, only the Park group [7] has successfully achieved precise individual crystal tailoring to create well-defined crystal facets, but has not yet established facet heterojunction along the transport direction or investigated the charge separation effects between the heterofacet. A strategy that employed by the Yana group [8], involving the preparation of perovskite phase heterojunctions (PHJs) using a hybrid deposition approach, along with the addition of stabilizers to fill voids in different phase structures, could be adopted (Figure S14). Similarly, the research of Zhao's group[8] on perovskite facet heterojunction solar cells demonstrates that a bilayer design, fabricated through a combination of spin-coating and evaporation, can effectively mitigate the issues caused by bulk facet heterogeneity.

Table S1. XRD-derived crystallographic indices, FWHM, and crystal sizes under different solvent conditions.

Solvent ratio (DMSO:NMP, v:v)	**hkl**	***2θ***	**FWHM**	**Crystal size (nm)**
90: 00	100	13.978	0.096	83.373
75: 15	100	13.984	0.098	81.672
60: 30	100	13.970	0.096	83.372
45: 45	100	13.962	0.089	89.929
00: 125	100	13.966	0.082	97.606
90: 00	111	24.322	0.117	69.459
75: 15	111	24.324	0.125	65.013
60: 30	111	24.301	0.111	73.210
45: 45	111	24.334	0.104	78.143
00: 125	111	24.340	0.108	75.250

Table S2. The Penetration depth of CuKα radiation at 8 keV in perovskite films at different incidence angles. The X-ray wavelength is 1.54 Å.

Incident angles (°)	Penetration depth (nm)
0.5	44
1.0	102
1.5	156
2.0	210
2.5	264
3.0	317
3.5	370
4.0	423
4.5	477
5.0	530

Table S3. Roles of solvent and intermediate phases in two-step method for orientation regulation.

Solvent	Precursor engineering	Preferred XRD peak	Orientation
DMF/DMSO	PbI_2•DMSO	(111)	Random
DMF/NMP	PbI_2•0.5DMF•0.5NMP	(100)	Random
DMF/DMSO/NMP	PbI_2•DMSO	(100)	Random
	PbI_2•0.5DMF•0.5NMP	(111)	(111)-dominant non-dominant (100)

Table S4. The physical and chemical properties of perovskite precursor solvents.

Solvent name	N,N-Dimethylformamide (DMF)	Dimethyl sulfoxide (DMSO)	N-methyl-2-pyrrolidone (NMP)
Chemical structure	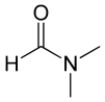	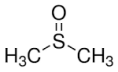	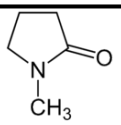
Boiling point (°C)	152.8	189	202
Vapor pressure (Pa)	516	55.6	39
Polarity (Debye)	3.86	5.87	4.20
Donor number (kcal mol^{-1})	26.6	29.8	27.3
Permittivity (ε_r)	36.7	47	32
Viscosity (mPa·s, 20 °C)	0.92	2.24	1.65
HLB index	11.6	12.4	8.2
Interaction energy with PbI_2 (eV)	-0.627	-0.840	-0.731
Interaction energy with FAI·PbI_2 (eV)	none	-2.138	-2.413
Solubility of PbI_2	~1M	~1.5M	~1.3M

Table S5. Detailed photovoltaic parameters of different condition PSCs based on champion devices.

Sample	Direction	V_{oc} (V)	J_{sc} (mA/cm^2)	FF (%)	PCE (%)	Hysteresis index
Control	Forward	1.093	25.03	76.58	20.96	4.423
	Reverse	1.112	25.01	78.87	21.94	
Target	Forward	1.065	23.64	75.66	19.06	5.690
	Reverse	1.095	24.08	76.60	20.21	

Note: the active area of each device is 0.04 cm^2.

References：

(1) Du, Y.; Wang, Y.; Wu, J.; Chen, Q.; Deng, C.; Ji, R.; Sun, L.; Tan, L.; Chen, X.; Xie, Y.; Huang, Y.; Vaynzof, Y.; Gao, P.; Sun, W.; Lan, Z. NaHCO3-Induced Porous PbI2 Enabling Efficient and Stable Perovskite Solar Cells. *InfoMat* **2023**, *5* (6), e12431. https://doi.org/10.1002/inf2.12431.

(2) Wang, C.; He, B.; Hui, W.; Su, Z.; Chen, L.; Du, W.; Zhang, L.; Zhang, J.; Fu, M.; Wang, H.; Sun, B.; Wen, W.; Wang, S.; Lou, L.; Hou, C.; Zheng, G.; Song, L.; Chen, Y.; Gao, X. Controlling Water for Enhanced Homogeneities in Perovskite Solar Cells with Remarkable Reproducibility. *Adv. Funct. Mater. n/a* (n/a), 2403690. https://doi.org/10.1002/adfm.202403690.

(3) Li, J.; Li, F.; Ma, X.; Li, J.; Liang, S.; Zhang, L. Effects of Heat Treatment on Microstructure and Mechanical Properties of an ECAPed Al–Zn–Mg–Cu Alloy. *Adv. Eng. Mater.* **2018**, *20* (9), 1701155. https://doi.org/10.1002/adem.201701155.

(4) Zhou, B.; Zhao, P.; Guo, J.; Qiao, Y.; Hu, S.; Guo, X.; Liu, J.; Li, C. Unlocking the Potential of Antisolvent-Free Perovskite Solar Cells: Modulating Crystallization and Intermediates through a Binary Volatile Additive Strategy. *Nano Energy* **2024**, *124*, 109487. https://doi.org/10.1016/j.nanoen.2024.109487.

(5) Lee, J.-W.; Dai, Z.; Lee, C.; Lee, H. M.; Han, T.-H.; De Marco, N.; Lin, O.; Choi, C. S.; Dunn, B.; Koh, J.; Di Carlo, D.; Ko, J. H.; Maynard, H. D.; Yang, Y. Tuning Molecular Interactions for Highly Reproducible and Efficient Formamidinium Perovskite Solar Cells via Adduct Approach. *J. Am. Chem. Soc.* **2018**, *140* (20), 6317–6324. https://doi.org/10.1021/jacs.8b01037.

(6) Huang, Z.; Bai, Y.; Huang, X.; Li, J.; Wu, Y.; Chen, Y.; Li, K.; Niu, X.; Li, N.; Liu, G.; Zhang, Y.; Zai, H.; Chen, Q.; Lei, T.; Wang, L.; Zhou, H. Anion–π Interactions Suppress Phase Impurities in FAPbI3 Solar Cells. *Nature* **2023**, *623* (7987), 531–537. https://doi.org/10.1038/s41586-023-06637-w.

(7) Ma, C.; Eickemeyer, F. T.; Lee, S.-H.; Kang, D.-H.; Kwon, S. J.; Grätzel, M.; Park, N.-G. Unveiling Facet-Dependent Degradation and Facet Engineering for Stable Perovskite Solar Cells. *Science* **2023**, *379* (6628), 173–178. https://doi.org/10.1126/science.adf3349.

(8) Ji, R.; Zhang, Z.; Hofstetter, Y. J.; Buschbeck, R.; Hänisch, C.; Paulus, F.; Vaynzof, Y. Perovskite Phase Heterojunction Solar Cells. *Nat. Energy* **2022**, *7* (12), 1170–1179. https://doi.org/10.1038/s41560-022-01154-y.